

Sunlight Induced Photocatalytic Degradation of Organic Pollutants by Biosynthesized Heterometallic Oxides Nanoparticles

Manviri Rani

MNIT Jaipur: Malaviya National Institute of Technology

Keshu Keshu

NITJ: Dr BR Ambedkar National Institute of Technology

Uma Shanker (✉ shankeru@nitj.ac.in)

Dr B R Ambedkar National Institute of Technology Jalandhar-Punjab, India <https://orcid.org/0000-0002-2448-3604>

Research Article

Keywords: Green synthesis, Heterometallic oxides, Photodegradation, Sunlight, Reusability

Posted Date: May 4th, 2021

DOI: <https://doi.org/10.21203/rs.3.rs-413408/v1>

License:  This work is licensed under a Creative Commons Attribution 4.0 International License.

[Read Full License](#)

Abstract

Extensive and widespread use of dyes and phenols with high persistence, bioaccumulation and suspected carcinogens have called for their removal. Seeing environmental-concern, green-efficient methodology based advanced nanomaterials are commanding. Herein, to overcome limitations of single metals, heterometallic oxides (HMOs) – CuFe_2O_4 , CuMn_2O_4 and MnZn_2O_4 have been prepared through a greener way involving *A. indica* (biogenic stabilizing and capping-agent). X-ray diffraction data revealed the crystalline-nature of HMOs nanospheres (particle size ≤ 100 nm) as visualized with electron microscopy. Subsequently, HMOs were evaluated for photoactivity for removal of 3-Amino Phenols (3-AP) and Eriochrome Black T (EBT) at various reaction parameters (pollutant: $50\text{--}130$ mgL^{-1} ; catalyst: $20\text{--}100$ mg; pH: $3\text{--}11$; dark-sunlight). All HMOs nanocatalyst at optimum-amount (80 mg) showed substantial degradation of 50 mgL^{-1} of 3-AP (85–93%) and EBT (80–95%) with slight difference of efficacy ($\text{CuFe}_2\text{O}_4 > \text{MnZn}_2\text{O}_4 > \text{CuMn}_2\text{O}_4$) under sunlight at pH ~ 7 . CuFe_2O_4 showed admirable photocatalysis due to high-surface-area (35.68 m^2g^{-1}), low band-gap (2.4eV), larger particle stability (-22.0 mV), and lower intensity observed in photoluminescence. Sharp decline curves indicated for first-order-kinetic fitted in Langmuir-adsorption ($R^2 \geq 0.92$; $p \leq 0.03$). Colour change was visually proved for both treated pollutants and HMOs reduced $t_{1/2}$ of 3-AP (0.9–1.7 h) and EBT (0.6–0.8 h) to the greater extent. Having less electronegative N-atom in the diazo functional-group, EBT degraded quickly than 3-AP (-OH directly connected with an aromatic nucleus). Scavenger-analysis substantiate the role of hydroxyl-radical in photodegradation studies. Reusability of HMOs for multiple uses ($n = 8$) without significant loss of activity advocated high-sustainability and cost-effectiveness. Finally, green synthesized HMOs nanoparticles with prominent surface characteristics were offer a viable alternative photocatalyst for industrial-applications.

1. Introduction

The release of poorly treated industrial effluents enriched with several recalcitrant chemicals, into freshwater resources is a serious threat to the entire ecosystem (Chong et al., 2010; Zeydouni et al., 2018; Villegas et al., 2019). The major class of pollutants is phenols which are used in petrochemicals, pharmaceuticals, resin manufacturing, and plastics while dyes are utilized in textile, paint, paper, fabric industries (Caetano et al., 2009; Liu et al., 2019; Tian et al., 2020). However, many phenols have been used as precursors or intermediate in the industrial manufacturing of organic dyes and pesticides. Degradation of phenols and their derivatives are quite difficult due to higher half-life ($t_{1/2}$: 15 to 72 days) and solubility (35 mg/mL) in water (San et al., 2001; Aimeur et al., 2020). Greater stability and toxicity of phenols and organic colorants (major leading pollutants) have resulted in hazardous exposure for all living beings even in very less quantity (Sas et al., 2020). They potentially act as endocrine disruptors because of easy absorption via the skin (Arques et al., 2007). The presence of amino phenols in water causes allergic reactions and respiratory diseases in humans (Tian et al., 2019). Distinguishing odor was produced by even minor exposure (5 mg L^{-1}). of chlorinated phenols which required removal on exceeding above the permissible limit set from $0.1\text{--}1$ mg L^{-1} in drinking water (Rachna et al., 2020). US-

EPA has categorized phenols in the list of top main concern pollutants beyond concentration level of $0.01 \mu\text{g L}^{-1}$ (Bagal et al., 2013; Li et al., 2018). Dyes are occupying chief portions of industrial effluent worldwide with the quantity of nearly 280,000 tons per annum (fabrics: 54%; paint: 8%; paper: 10% and dyeing: 21%) (Ghaly et al., 2014; Hanafi and Sapawe, 2020). Eriochrome Black T (EBT) (Sodium 1-[1-hydroxynaphthylazo]-6-nitro-2-naphthol-4-sulfonate) dye, anionic with an azo functional group, extensively used for silk textile (Barka et al., 2011). and in various Institutional laboratories to identify the hardness of water (0.05-0.08g as an indicator) (Kansal et al., 2013). The physico-chemical properties of EBT and 3-AP are highlighted in Table 1. Due to the high toxicity of omni-persistent organic pollutants, there is an urgency to develop low energy, easy to handle and cost-effective based state-of-the-art techniques for their detection and complete removal from water (Pitarch et al., 2010). Traditional methods (adsorption, filtration, coagulation, membrane separation) have lost their ground due to merely mass transfer of pollutants and other practical restrictions (Mukherjee et al., 2018). To overcome the hurdle associated with old methods, nanomaterials based photocatalysis (Semiconductor assisted degradation) is being widely promoted cum accepted for combating pollution credited to the most promising and adorable characteristics of the economy and mild reaction conditions with less energy consumption (Rani et al., 2017; Rani et al, 2018a). Transition metal oxides have peculiar properties high thermal stability, inherent oxidation state and economics (Mathew et al., 2011). ZnO and TiO_2 (popular nanoparticles) have shown encouraging performance in photocatalysis and industries but their extensive use is causing bioenrichment in the ecosystem. Moreover, a large bandgap ($> 3\text{eV}$) requiring high UV energy for excitation and recombination of charges are putting pressure on researchers to develop new/alternative or modified nanomaterials with improved properties. Doping the surface of metal oxides or coupling with metals, non-metals or transition metals compounds shift bandgap energy level towards the visible region and also prevent charge recombination due to introductory-additional energy level of dopant (Rachna et al., 2018; Heinz et al., 2000; Watanabe et al., 2000). In light of those observations, nanoparticles of SnO_2 (Honarmand et al., 2019), CeO_2 (Mishra et al., 2018), Bi_2WO_6 (Lai et al., 2019), $\text{Zn}_{0.3}\text{Al}_{0.4}\text{O}_{4.5}$ (Fegadae et al., 2020), $\text{Co-Co}_3\text{O}_4$ (Adekunle et al., 2019), SrFe_2O_4 (Zafar et al., 2018) for the elimination of EBT; and CuO (Nayak et al., 2020), CeO_2 (Ahmad et al., 2020), Ni-ZnO (Sharma et al., 2016), $\text{CuFe}_2\text{O}_4@\text{r-GO}$ (Othman et al., 2019) and peroxymonosulfate activated $\text{CuO-Co}_3\text{O}_4@\text{MnO}_2$ (Khan et al., 2017) for phenols were employed. Superparamagnetic magnesium ferrite and $\text{MgFe}_2\text{O}_4@ \gamma\text{-Al}_2\text{O}_3$ were used for the removal of renowned organic dyes (Atrak et al., 2018). However, some of the above-mentioned absorbents were reported with UV-light exposure.

Synergistic effects of various bi-or trimetallic nanoparticles of 3d-series synthesized via greener route containing gel, gum or plants have been reported (Farood et al., 2017; Farood et al., 2017a; Sorbiun et al., 2018). Spinel (AB_2O_4) nanoparticles are frequently utilized due to fascinating physicochemical and structural characteristics as well as environmental safety (Zhao et al., 2017). Cu replace M^{2+} cations in MFe_2O_4 which magnified catalytic property even at low temperature (Wang et al., 2019). Cu^{2+} ion shows Jahn-Teller distortion and charges redistribution which generates a transfer of electron (Nedkov et al., 2006; Liu et al., 2016). As revealed from the published document, there is no data about green synthesis

and subsequent comprehensive photo-application of CuFe_2O_4 , CuMn_2O_4 and MnZn_2O_4 nanoparticles for degradation of selected toxic phenols and dye under sunlight. Adoption of the green process is appreciable because of its quickness, usage of plants, fabrications of highly pure (free from contaminants), and quantity enriched product while avoiding intermediate base groups and costly equipment and precursor. Plant parts have been hired for bio-reduction assisted production of several nanomaterials because of reducing cum capping and stabilization properties. Due to environmental concern, sunlight was preferred instead of UV-irradiation as polluted water face natural condition.

These facts embolden us for investigations on the synthesis of sunlight active nanoparticles of CuFe_2O_4 , CuMn_2O_4 and MnZn_2O_4 by using leaves of *Azadirachta indica* and subsequent applications for potential degradation of toxic 3-AP and EBT in water. Phytochemicals (alkaloids and terpenoids) present in *A.indica* lesser down interfacial tension to regulate nucleation/ agglomeration of nanomaterials during the fabrication process (Rani et al., 2018b;Rani et al., 2020). Besides, toxicity and bioaccumulation, the selection of pollutants was based on the quantity of these pollutants used in the industries. Diverse parameters of contaminant concentration, nanocatalyst amount, pH, radiation environment and contact time were investigated to bring off the highest degradation. Langmuir isotherm and degradation pathways were studied to investigate the adsorbing behavior and types of metabolites formed. Reusability studies were also investigated for confirmation of the sustainability of nanomaterials. Scavenger analysis was explored to find out the role of free radicals under sunlight.

2. Experimental

2.1. Materials

Metal salts namely $\text{Cu}_2(\text{NO}_3)_2$, $\text{Mn}(\text{NO}_3)_2$, $\text{Zn}(\text{NO}_3)_2$, $\text{Cu}_2(\text{NO}_3)_2$, $\text{Fe}_2(\text{NO}_3)_2$, liquid NH_3 were procured from Hi-Media, India. Standard of 3-Aminophenol and Eriochrome Black T dye were purchased from Merck, Germany. Fresh leaves of *A. indica* were collected from a tree in our institute campus, washed and crushed in a pestle mortar. The green color liquid of *A. indica* extract was filtered and kept at 4°C in refrigerator for further experimental work of nanoparticles synthesis. All the solutions were prepared in deionized water.

2.2 Design of green experiment for HMOs nanomaterials

As shown in Fig. 1, HMOs were synthesized via co-precipitation method involving leaf extract. Solutions of different metal salts (0.1M, 100mL) in water were prepared by adding 5 mL of *A. indica* plant extract in each solution. The solution of one metal salts was mixed into another by dropwise addition under 2h of constant stirring at 80°C . Liq. ammonia was added slowly in the reaction mixture until the precipitation was formed at the bottom of the beaker and kept the product undisturbed for 12h. The obtained precipitate was washed multiple times and then kept in an oven at 70°C for drying. For complete dehydration, crystals were muffled at 400°C for 4 hours, crushed, grind, and kept for further use.

Synthesized HMOs were analyzed by powder X-ray diffraction (p-XRD), microscopy (FE-SEM and TEM), Spectroscopy (FT-IR and XPS), UV- spectrometer (UV-reflectance), photo-luminescence, Zeta-sizer, and BET. The details belong to instrumentation have been presented in the supplementary information.

2.3 Photodegradation of 3-AP and EBT by using nanocomposite of HMOs from spiked water

In glass vials, photodegradation studies of targeted organic pollutants with synthesized HMOs were carried out. The batch experiment consisted of 25 to 125 mgL⁻¹ of 3-AP and EBT solution, catalyst quantity changed from 20 to 100 mg along with diverse pH (3–11) and reaction time. In the availability of direct sunlight, degradations of 3-AP and EBT with HMOs nanocomposite in spiked de-ionized water with a definite amount of targets. For a better understanding of the effect of sunlight on degradation, the samples were also investigated in dark conditions. To maintain pH of reaction mixture borax (borax; 0.025M + NaOH; 0.1M) and citrate buffer (citric acid; 0.1M + trisodium citrate; 0.1M) was used. The reaction continued for 5 h for 3-AP and 3h for EBT dye in presence of sunlight and the adsorption capacity of the nanocatalysts was also found out in the dark. Underdeveloped conditions, individual feigned samples of water were kept under daylight irradiation for 5 h (11.00 am to 4:00 pm). During the reaction, average temperature (°C) was 29 ± 1.7 (range: 28.0–35.0) and the intensity of sunlight was 452 ± 183 W/m² (range: 151–812) as measured with a pyranometer. Subsequently, the supernatant of the reaction mixture was taken out in triplicate for quantitative (Ultra-Violet-Spectrophotometer) and qualitative (Gas Chromatography-Mass Spectrometric) analysis. Blank samples of contaminants EBT and 3-AP (short of nancatalyst) were also tested to examine the degradation efficiency of HMOs. Comparison the results obtained from samples place under dark conditions further confirms the role of natural sunlight in degradation. The degradation efficiency (%) was estimated: $(C_{\text{initial}} - C_{\text{final}}) / C_{\text{initial}} \times 100$. Other factors like the amount of catalyst, initial concentration of selected pollutants and initial pH of the solution were optimized.

2.4 Statistical analysis

The kinetics study and statistical treatment of experimental data for the present application studies on removal of targeted contaminants by HMOs were performed empirically from asymptotical analysis by Sigma Plot Systat. Outcomes were inconsistent with the triplicate study. Microsoft excels program was employed for the calculation of the standard deviation of the triplicates. Experimental significance was analyzed by comparing the results through beta coefficient (R^2) and probability values (p -values). Fit equations were used for kinetics and adsorption data.

3. Results And Discussion

3.1. Morphological and structural analysis

3.1.1 PXRD

Crystallinity, composition and structure of HMOs nanocomposite were determined from PXRD, PAN analytical X-PERT Pro (Fig. 2). The purity and crystallinity of HMOs were observed by the lack of diffraction peaks and the presence of sharp peaks (Rani et al., 2020). Slightly shift in PXRD parameters in HMOs as compared to parent nanomaterial confirmed the doping of both metal oxides. The maximum intensity and miller indices observed at 2θ values: 36° (311), 33.2° (310) and 66.2° (440) for CuFe_2O_4 (Sreekala et al., 2020); 35.6° (220), 30.2° (311), 18.2° (111) and 43.3° (222) for CuMn_2O_4 ; and 36.2° (111), 32.5° (110), 29.1° (011) and 17.8° (111) for MnZn_2O_4 with slight shifting of peak position from each other. Parental peak reflection observed at 2θ of 35.6° (CuO: monoclinic crystal phase having space group C2/c) (Etefagh et al., 2013), 35° (Fe_2O_3 : high-intensity peak, semi-crystalline) (Rachna et al., 2018), 29.1° (crystalline MnO_2) (Jana et al., 2007) were also supported HMOs formation. The major peak at 29.1° and slight shifting from angles 31° , 33° and 36° from parent nanomaterial (ZnO) confirmed the doping of MnO_2 and ZnO (Fig. 3S). The average crystalline size (d_c) was determined correspond to the most intense peak by using Scherer's equation $d_c = K\lambda/\beta\cos\theta$ (Klug., 1974). Predicted crystalline sizes of CuFe_2O_4 , CuMn_2O_4 and MnZn_2O_4 were 6.63nm, 10.25nm and 12.31 nm. Smaller average crystalline size of CuFe_2O_4 nanoparticle as compared to other HMOs nanomaterials supported the good adsorbing properties.

3.1.2 FT-IR

FT-IR analysis confirmed the structural composition and bonding between elements of different parent nanoparticles of HMOs nanocomposites as shown in Fig. 2. Two adsorption bands in CuFe_2O_4 observed at 607 cm^{-1} (Fe-O bond in octahedral) and 470 cm^{-1} (Cu-O bond in tetrahedral sites) confirmed the incorporation of two metal oxides (Sreekala et al., 2020; Tehrani, 2012). In pure CuO, spectra were narrow bands at 457 , 526 , 600 , and 784 cm^{-1} confirm the formation of CuO nanoparticles (Sukumar et al., 2020). An absorption band near 622 cm^{-1} was assigned to vibration of Fe-O bond in iron oxide (Rufus et al., 2016). Similarly, two stretching frequencies were observed in CuMn_2O_4 nanocatalyst at 509 cm^{-1} (Cu-O), 500 cm^{-1} (Mn-O) as well as in MnZn_2O_4 at 525 cm^{-1} (Zn-O) and 620 cm^{-1} (Mn-O). The peak at 520 cm^{-1} arises from the stretching vibration of the Mn-O in pure MnO_2 (Liang et al., 2008; Olmos et al., 2005) and the peak at 459 cm^{-1} confirms the ZnO bond at bending vibration (Dhanemozhi et al., 2017). The slight shift of peaks towards lower or higher frequency as compared to parent nanomaterial revealed the formation of HMOs. The bands of C-O, C-C, C = C and C-H are attributed to alkanes, alkenes, alcohols and carboxylic acid (Fig. 2). The observed functional groups in the FTIR study confirmed that the phytochemicals (proteins, phenolics alkaloids and flavonoids) were involved in the formation and stability of green synthesized HMOs nanoparticles (Rajkumar et al., 2018; Rufus et al., 2016). The very minor peaks nearly at 3400 cm^{-1} in all three HMOs might be due to the surface acidity of hydroxyl (-OH) functional groups (Rani et al., 2020). The FT-IR analysis confirmed the doping of two HMOs present in nanocatalyst might be bonded with oxygen element.

3.1.3 Microscopic techniques

FE-SEM

Surface morphology and structure of synthesized nanoparticles were examined by electron microscopic analysis. Nanospheres of CuFe_2O_4 (Fig. 2a), CuMn_2O_4 (Fig. 2d) and MnZn_2O_4 spinels with rough surface were seen in FE-SEM image (Fig. 2g). Literature survey is revealing nanoflower of ZnO, nanorods of Fe_2O_3 and nanospheres of CuO and MnO_2 formed by green methods (Ramzan et al., 2020; Rani et al., 2017; Rachna et al., 2019; Rachna et al., 2018). Different geometry of HMOs than individuals (nanoflower of ZnO, nanorods of Fe_2O_3 and nanospheres of CuO and MnO_2) reported earlier by green methods, further confirmed their interaction (Fig. 3S). FE-SEM (Fig. 2) results were also supported with EDS which explains the elemental composition (%) of variable atoms in HMOs spinel's nanoparticles i.e. Cu, Fe and O with 11.44%, 58.71% and 29.85%, respectively in CuFe_2O_4 ; Cu (7.51%), Mn (66.13%), O (25.10%) in CuMn_2O_4 and Mn (28.22%), Zn (47.74%) and O (23.13%) in MnZn_2O_4 . From FESEM-EDS it was confirmed that the convenient synthesis path reported here provides easy, economical and environment friendly HMOs nanocatalyst.

TEM

For depth information of internal framework, morphology and crystallinity of HMOs nanocomposites, HR-TEM analysis was carried out (Fig. 4a,b,c). The spherical shape of HMOs (size less than 50 nm) supported the results of FE-SEM. It can be observed that agglomerates are formed by a superposition of nanometric size particles in the case CuFe_2O_4 and CuMn_2O_4 . Literature survey revealed the spherical morphology of iron oxide (Karade et al., 2019), CuO (Chowdhury et al., 2020) and MnO_2 (Wang et al., 2017). The TEM images of ZnO confirm that the particles are almost hexagonal with slight variation in thickness (Geetha et al., 2016). After incorporation of one metal oxide into another slight change in morphology as well as particle size was observed. MnZn_2O_4 has smaller size spherical particles as compared to parent nanomaterials with minor variation in morphology as shown in TEM image (Fig. 4c). Selected Area Electron Diffraction (SAED) pattern shows bright concentric rings which revealed high crystallinity of HMOs and show good agreement with the XRD diffractogram of supported the PXRD results. The size histogram shows the smaller size of CuFe_2O_4 within range of 6–8 nm, 8–10 nm in CuMn_2O_4 and 10–13 nm in MnZn_2O_4 . Selected Area Electron Diffraction (SAED) pattern showed bright concentric rings of high crystalline HMOs and shows good agreement with the XRD diffractogram of supported the PXRD results. The size histogram shows the smaller size of CuFe_2O_4 within the range of 6–8 nm, 8–10 nm in CuMn_2O_4 and 10–13 nm in MnZn_2O_4 . These TEM observations confirm the small size of the HMOs and the obtained values are in good agreement with the size of crystallites calculated from the Scherrer equation. From microscopic studies, it was confirmed that the convenient synthesis path reported here provides easy, economical and environment-friendly HMOs nanocatalysts.

3.1.4 XPS

The surface chemical compositions of synthesized nanoparticles (valency and interaction between constituent elements) were determined with XPS analysis that confirmed the presence of all elements in

agreement with EDS (Fig. 5). As shown in the spectrum, the peak of Cu $2p_{1/2}$ and Cu $2p_{3/2}$ were observed at 953.0 and 933.0 eV considered as characteristic peaks for Cu $^{+2}$ ions (Faungnawakij et al., 2009). The characteristic peaks of Fe $^{+3}$ were observed at the binding energies of 723.6 and 709 eV (NuLi et al., 2004). However, in zinc spectrum peaks at 1020eV and 1045eV recorded corresponding to Zn $2p_{1/2}$ and Zn $2p_{3/2}$, respectively. A similar trend was also observed in ZnO with minor differences due to interfacial interaction between nanocomposites (Al-Gaashani et al., 2013; Han et al., 2014). The manganese element presents in MnZn $_2$ O $_4$ and CuMn $_2$ O $_4$ HMOs nanocatalyst shows the characteristic peak at 640.0 eV and 652.5eV. The O1s peak which is common in all three HMOs shows a characteristic peak at 528eV (Xue et al., 2004). The C1s were added as references during the measurement process. By combining both EDS and XRD observations, it can be confirmed that the HMOs nanocatalyst was successfully synthesized by green method.

3.1.5 BET Surface area

Surface characterization of synthesized HMOs and individual nanomaterials was investigated by BET gas isotherms where nanomaterials were exposed to enhanced pressure of nitrogen gas adsorption. Surface areas of the HMOs revealed that CuFe $_2$ O $_4$ (35.7 m 2 g $^{-1}$) has the largest surface area followed by CuMn $_2$ O $_4$ (30.6 m 2 g $^{-1}$) and MnZn $_2$ O $_4$ (10.2 m 2 g $^{-1}$) (Fig. 1S). The obtained results were also compared with the unaccompanied metal oxides surface area (CuO: 17.629 m 2 g $^{-1}$, Fe $_3$ O $_4$: 8.992 m 2 g $^{-1}$, ZnO: 8.45 m 2 g $^{-1}$, MnO $_2$: 13 m 2 g $^{-1}$) (Rani et al., 2018; Ramimoghadam et al., 2013; Kadam et al., 2018). As expected, the surface area of HMOs larger as compared to unaccompanied metal oxides due to synergistic phenomenon which is conducive to enhanced its textural characteristics (Rani and Shanker, 2020a).

3.1.6 Reflectance spectra and band gap analysis

UV-Vis reflectance spectra data (by UV-Vis spectroscopy) was used to get the band gap (E_g) of synthesized HMOs nanoparticles by direct transition Tauc equation.

$$(\alpha h\nu)^2 = A(h\nu - E_g)$$

Here, α is optical absorption coefficient

h is Planck's constant

ν is the frequency of incident radiation,

A is a constant and E_g is the energy gap.

The direct transition in method was justified with exponent 2 value. The extrapolating of the linear portion of the curve to zero adsorption values in $(\alpha h\nu)^2$ v/s photon energy graph resulted in band gap energy (Inamuddin, 2019). The bandgap energy values were- CuFe $_2$ O $_4$ (2.1 eV), CuMn $_2$ O $_4$ (2.4eV) and MnZn $_2$ O $_4$

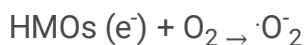
(2.6eV) as shown in Fig. 6(a). From literature survey band gap of Fe_2O_3 (2.23 eV) (Rachna et al., 2018), CuO (4.2 eV) (Arun et al., 2015), MnO_2 (2.6 eV) (Vijayalakshmi et al., 2019) and ZnO (3.3 eV) (Rachna et al., 2020). Synergic effect via the introduction of different metal oxides and displacement of the transmittance edges to the lower region might be responsible for this occurrence (Rani et al., 2018; Rani and Shanker, 2018c). The lower band gap has enhanced photocatalytic activity and is used for commercial applications. Lower band gap values are advantageous for harvesting light energy (natural sunlight) in viable use. The complete characteristics of green synthesized HMOs were explained in Table 2.

3.2 Estimation of photocatalytic activity for HMOs in degradation of 3-AP and EBT dye

To investigate photocatalytic efficiencies of HMOs against 3-AP and EBT dye different batch study were evaluated having the amount of pollutant (50 to 150 mg L^{-1}) with variation in HMOs dose (20 – 100 mg), pH (3 – 11) and exposure (sunlight and dark) (Fig. 7a,b). It is important to mention that all the other parameters were kept constant while changing another one. The maximum degradation was obtained at a minimum concentration of 3-AP and EBT (50 mg L^{-1}), definite nanocatalyst amount (80 mg) and pH (~ 7) under sunlight exposure. The presence of higher amount of pollutant molecules reduces the occurrence of photogenerated charged species (Rani et al., 2017a; Rani et al., 2017b; Satheesh et al., 2014). The degradation was lowered at a higher quantity due to insufficient hydroxyl radicals to degrade a large number of molecules of the organic pollutant. However, for cost-effectiveness dose depended study was investigated by varying the amount 20 – 100 mg L^{-1} . Maximum degradation was observed at 80 mg and decreases afterward due to collisions in-between reaction mixture charged and uncharged particles deactivated the catalyst (Fig. 7c,d) (Rachna et al., 2019a).

At neutral pH, maximum photodegradation was achieved for 50 mg L^{-1} of 3-AP and EBT with a definite catalytic dose (80 mg) (Fig. 7e,f). Decrease in degradation because of the ion screening effect caused by H^+ and OH^- ions in acidic and basic solution (Shanker et al., 2017). In acidic pH, the pollutant and nanocatalysts are neutral due to which H^+ use most of the electrons. HMOs depicted good photoactivity at neutral pH because HMOs generally have a point of zero charge (Pzc) nearly 6. Hence, zeta potential of HMOs was investigated at neutral pH. Moreover, 3-AP and EBT pollutants contain π -electron density due to which formation of “cation- π ” complexes after networking with a positively charged surface of nanocomposite at neutral pH. The surface charge of the HMOs plays a significant role in degradation efficiency at various pH. The calculated zeta potential at neutral pH are : -23.1 mV , -22.7 mV and -20.5 mV for CuFe_2O_4 , CuMn_2O_4 and MnZn_2O_4 , respectively (Fig. 6g,h,i). Among the HMOs nanocomposites used, CuFe_2O_4 and CuMn_2O_4 having a large value of zeta potential (higher surface stability) which minimized the aggregation of the nanoparticles (Shanker et al., 2016). The maximum capacity for CuFe_2O_4 is supported by its negative potential value showed stability and larger repulsion amongst the particles (Mu et al., 2001; Lin et al., 2008; Rani et al., 2018).

For comparison study, removal of 3-AP and EBT pollutants were studied under sunlight and dark condition. The reaction mixture contains 50 mg L⁻¹ of organic pollutants and 80 mg catalytic dose, with CuFe₂O₄, CuMn₂O₄ and MnZn₂O₄ separately, at neutral pH exposed to natural sunlight. Photodegradation of 3-AP was found: 93 % (CuFe₂O₄), 90 % (CuMn₂O₄) and 85% (MnZn₂O₄) under sunlight and 47% (CuFe₂O₄), 39% (CuMn₂O₄) and 30% (MnZn₂O₄) in dark (Fig. 8i). However, EBT dye degraded to larger extent: 97 % (CuFe₂O₄), 95 % (CuMn₂O₄) and 80% (MnZn₂O₄) under sunlight and 55% (CuFe₂O₄), 45% (CuMn₂O₄) and 35% (MnZn₂O₄) in dark condition. In presence of sunlight large number of reactive species was formed lead to the degradation of organic pollutants. Active species i.e OH and O₂ radicals are produced due to interaction between charge carriers (electron and hole pairs) and H₂O/O₂ in the reaction mixture. The lower band gap of HMOs results in a rapid excitation phenomenon. The life span of charge carriers is the key factor in the photocatalytic degradation phenomenon (Fig. 6d,e,f). The Photoluminescence (PL) spectroscopy technique is used for the determination of proficiency of trapping, recombination probability of charge carrier and transmission in a semiconductor. Due to the photoexcited of electron and hole, the PL spectra were obtained. Lesser PL emission intensity results in swift transport and separation of charge carriers upsurges. To get the emission spectra of the nanocatalyst, the excitation wavelength has been set at 300nm at room temperature. This selected wavelength must be larger compared actual bandgap. Supreme intensity peak observed in HMOs in between 300–400 nm. CuFe₂O₄ has lesser emission intensity as compared to others which shows a lesser recombination rate of electron-hole pairs and shows better photocatalytic capacity. The reason behind the acceleration in recombination of charge carriers was doping of different metal oxides causes electron donor and electron acceptor participation among these (Meng et al., 2011; Zhong et al., 2014; Ma et al., 2018; Rani et al., 2020). These reactive species convert the complex structure of organic pollutants (3-AP and EBT) into smaller and safe metabolites analyzed by using GC-MS. To support this fact lower activity of HMOs nanocatalysts under dark conditions and very minor degradation with blank samples (7% of 3-AP; 10% of EBT). The incorporation of two different metal oxides having different bandgap leads to the generation of charge carriers present in the transition band for more time and leads to the huge production of OH radicals for degradation (Rani et al., 2018). The main advantage of using sunlight as an irradiation source for the degradation of many pollutants are environment friendly, easy availability, cost-effectiveness and catalyst does not decompose during the procedure. Mechanism followed by HMOs for the degradation of organic pollutant could be explained by the equations:



OH· + Pollutant → Degraded smaller by-products

In presence of optimized conditions, CuFe₂O₄ shows maximum degradation (3-AP 93%; EBT 97%) followed by CuMn₂O₄ (3-AP 90%; EBT 95%) and MnZn₂O₄ (3-AP 85 %; EBT 90%) under sunlight. The maximum degradation showed by CuMn₂O₄ supported by the lower bandgap (2.1 eV), largest surface area (35.7 m²g⁻¹), negative zeta potential (-23.1 mV) and lower intensity in photoluminescence (PL). The faster degradation of EBT dye as compared to 3-AP due to the presence of lesser electronegative nitrogen as compared to oxygen in 3- AP. However, 3-AP has a more stable structure as compared to EBT due to the smaller aromatic structure.

4. Proposed Chemical Kinetics

In presence of optimized conditions (50 mgL⁻¹ of organic pollutant, 80 mg of HMOs, neutral pH and sunlight), rapid degradation of 3-AP (93 % by CuFe₂O₄, 90 % by CuMn₂O₄, 85% by MnZn₂O₄) in 5h and EBT (97 % by CuFe₂O₄, 95 % by CuMn₂O₄, 80% MnZn₂O₄) in 3h followed first-order kinetics. Maximum degradation of was observed by CuFe₂O₄ is justified by the highest k value (Table 3) (Figure b(i), b(ii)). The amount of organic pollutants (3-AP; EBT) left after 2h were: (3-AP 0.57 ± 0.003 mgL⁻¹; EBT 0.330 ± 0.002 mgL⁻¹), (3-AP 0.721 ± 0.002 mgL⁻¹; EBT 0.600 ± 0.001 mgL⁻¹), (3-AP 0.820 ± 0.002 mgL⁻¹; EBT 0.810 ± 0.002 mgL⁻¹) in the presence of CuFe₂O₄, CuMn₂O₄, and MnZn₂O₄, respectively. As compared to blank, half-life (t_{1/2}) of AP and EBT decreases up to 6–10 times with HMOs were concluded about good photodegradation potential of nanocatalyst. Photodegradation started with adsorption of dye on nanocatalyst and fitted to Langmuir isotherm as shown in Fig. 7(i-l). For the comparison study, other adsorption models were also investigated i.e Freundlich, Sips, Dubinin–Radushkevich (DRK) (Fig. 2S) and Temkin model. The Langmuir constants X_m (maximum amount of pollutant adsorbed in mg g⁻¹), k_L(dm³ mol⁻¹) and R² for 3-AP were attained in the order: CuFe₂O₄ (2.0; 0.22; 0.95) > CuMn₂O₄ (1.92; 0.36; 0.98) > MnZn₂O₄ (1.61; 0.39; 0.99). In case of EBT, these values were found to be: CuFe₂O₄ (2.48; 0.36; 0.912) > CuMn₂O₄ (2.04; 0.52; 0.95) > MnZn₂O₄ (1.86; 0.61; 0.97). The statistical data of different isotherms shown in Table 1S. Hence, maximum dyes adsorption was found with CuFe₂O₄ HMO due to larger surface area and negative zeta potential as compared to the other HMOs.

5. Photodegradation Pathways Of 3-ap And Ebt By Using Hmos

Gas Chromatograph-Mass Spectrometer (GC-MS) technique was employed for the sample of 3-AP and EBT (Concentration: 50 mgL⁻¹, Catalytic amount: 20mg, pH~7) of 5h degradation time. Results showed that the initial degradation of pollutants on the surface of catalyst converted into less stable products that further mineralized into a safer product according to the mass spectrum (Fig. 10). The mass spectra of EBT and 3-AP were interpreted by use of NIST-library installed in the software of the GC-MS and reported literature information. The OH· is the major cause of the degradation of the complicated compounds into smaller and safer metabolites.

Based on GC-MS results, pathway degradation was drawn as shown in Fig. 11 and concluded that hydroxyl radical attack on the azo group present in EBT dye and results in the formation of unstable intermediates 2-Nitronaphthalene ($m/z = 73$) and Naphthalene-1-ol ($m/z = 141$). Advanced oxidations phenomenon led the benzene-1,2,3-triol ($m/z = 128$) as by-product. However, the total Ion Chromatograph (TIC) (Fig. 9) revealed that benzene-1,2,3-triol ($m/z = 128$) is short living species. Due to ring-opening and oxidation process, product (1E,3Z)-hexa-1,3,5-trien-1-ol ($m/z = 98$) was formed and further breakdown into (E)-prop-1-en-ol ($m/z = 59$). Further presence of excess hydroxyl radicals converted toxic molecules into mineralization of end products (Rachana et al., 2020). The toxic molecule 3-AP degraded due to advanced oxidation process into ((2E,4Z)-3-hydroxyhexa-2,4-dien-1-ylidene) amino) oxonium ($m/z = 127$) and phenol ($m/z = 95$) (Fig. 11b). Further hydroxyl attack and ring opening led to formation of pent-1-en-3-one ($m/z = 86$) and (E)-3-aminoprop-1-en-1-ol ($m/z = 73$) was reported in literature. The TIC of 3-AP confirmed that these products were short living and due to the presence of excess hydroxyl radical formation of safer mineralized products as shown in Fig. 11b (Rani et al., 2020).

The scavenger analysis was investigated to endorse the function of hydroxyl radical in photodegradation of EBT and 3-AP. The discrete quenchers: ethanol, triethanolamine and benzoquinone were utilized for hydroxyl radical, h^+ , O^{2-} , respectively for quenching of radicals. As a result, the decline in degradation was observed when the sample containing radical quenchers (Fig. 8 (ii)). Hence, results concluded that the active hydroxyl radicals are a major reason for the degradation of EBT and 3-AP. Moreover, for a better understanding of photodegradation, PL was carried out which related to their charge recombination.

6. Comparison With Other Catalysts

The toxic and carcinogenic nature of EBT and 3-AP towards living beings has motivated to investigate the eradication of both pollutants using nanomaterials (Table 4). It was revealed that only a few efficient studies are available while the procedure involved was uneconomical and unfriendly for the environment. Majorly, UV light is used for the removal of both pollutants which is not workable for the cure of industrial wastewaters. Sunlight active HMOs nanomaterials have not been explored so much in this area. However, in sunlight, both UV and visible light are present which is a cost-effective and technically feasible method for removal of EBT and 3-AP. The efficiency of synthesized HMOs showed 97% degradation of EBT and 93% of 3-AP in water under the exposure of sunlight into the safer and minor mineralized product. Moreover, the deployment of un-conventional nanomaterials should be helped to avoid the bio-enrichment of the exact recycled nanocatalyst. Overall, green synthesized HMOs supported the utilization of natural material in favor of green chemistry.

7. Reusability Of The Hmos

To find out the sustainability, cost-effectiveness, stability and recycle of fabricated HMOs, investigation reusability was performed. The HMOs were used during the experiment were recovered via filtration, washed by using acetone as well as with deionized water and dried in the hot air oven for reused in consequent cycles. Eight-time reusable in photocatalytic degradation of 3-AP and EBT with an initial

amount 50 mgL^{-1} were used to study the durability of the nanocatalyst. The result certified that HMOs depicted good efficiency upto eight cycles without any loss in photoactivity (Fig. 12a). However, percentage degradation was reduced might be because of the agglomeration of EBT or 3-AP on the surface of the catalyst. The higher stability and reusability of HMOs were supported by the PXRD patterns which do not show any significant change in the pattern as shown in Fig. 12b.

8. Conclusion

Establishment of a facile, inexpensive, recyclable, eco-friendly and highly efficient method for synthesis of HMOs nanosphere CuFe_2O_4 , CuMn_2O_4 and MnZn_2O_4 using *Azadirachita indica* as leaf extract in high yield. At optimized conditions, CuFe_2O_4 nanocatalyst showed maximum degradation (3-AP 93%; EBT 97%) as compared to CuMn_2O_4 (3-AP 90%; EBT 95%) and MnZn_2O_4 (3-AP 85%; EBT 80%) under direct exposure of sunlight through the semiconducting mechanism. Percentage degradation of pollutants depends on the negative zeta potential, superior surface area and low band gap. Langmuir adsorption isotherms and first-order kinetics has been followed majorly in the degradation process. The photocatalytic degradation of EBT and AP followed first-order kinetics. GC-MS analysis revealed that the complex structure of EBT dye breakdown into minor and non-toxic metabolites. The by-product (E)-Prop-1-ene-1-ol obtained in the case of EBT while in 3-AP prop-1-en-3-one and (E)-3-aminoprop-1-en-1-ol were formed after hydroxyl attack at the less hindered site. These products were finally mineralized. The possible pathway of both pollutants has also been proposed. The HMOs nanocatalyst was found to be reusable upto 8th cycle. This high reusability supports the sustainability of such nanostructures. According to the promising photocatalytic efficiency exhibited work, the CuFe_2O_4 , CuMn_2O_4 and MnZn_2O_4 nanospheres photocatalysts are expected to play a significant role in environmental purification by employing natural sunlight.

Declarations

Acknowledgement

One of the author Dr Manviri Rani is grateful to DST-SERB, New Delhi (Sanction order no. SRG/2019/000114) and TEQIP-III, MNIT Jaipur, India for the financial assistance. Dr Uma Shanker wishes to thank TEQIP-III, NIT Jalandhar, for financial support. Ms Keshu is thankful to Ministry of Human Resources and Development (MHRD) New Delhi for research fellowship.

Ethics approval and consent to participate: Not applicable

Consent for publication: Yes; all authors have full consent

Availability of data and materials: Data of manuscript will be made available on request

Competing interests: There are no financial and non-financial competing interests among authors

Funding: All the funding's have been fully acknowledged in the manuscript

Authors' contributions: MR visualized, Writing - original draft, Investigation in the manuscript. US supervised, Writing - review & editing the manuscript. Keshu performed Data curation, Software, Validation.

Acknowledgements: All the acknowledgments have been mentioned

References

1. Adekunle A S, Oyekunle J A O, Durosinmi L M, Oluwafemi O S, Olayanju D S, Akinola A S, Ajayeoba T A (2020) Potential of cobalt and cobalt oxide nanoparticles as nanocatalyst towards dyes degradation in wastewater. *Nano-Struct Nano-Objects*, 21:100405-100418. [org/10.1016/j.nanoso.2019.100405](https://doi.org/10.1016/j.nanoso.2019.100405)
2. Aimeur, M., Baudu, M., Zermane, F., Joussein, E., Bouras, E., O.,2020. Evaluation of the use of free or supported phenalenone based on natural halloysite for phenol photodegradation in aqueous solution, *J Photochem Photobiol A*, 404, 112904-112911. [org/10.1016/j.jphotochem.2020.112904](https://doi.org/10.1016/j.jphotochem.2020.112904)
3. Al-Gaashani R, Radiman S, Daud AR, Tabet N, Al-Douri Y (2013) XPS and optical studies of different morphologies of ZnO nanostructures prepared by microwave methods, *Ceram Int*, 39: 2283-2292.
4. Alharbi O M L (2018) Sorption, kinetic, thermodynamics and artificial neural network modelling of phenol and 3-aminophenol in water on composite iron nano-adsorbent. *J Mol Liq*, 260:261–269. [org/10.1016/j.ceramint.2012.08.075](https://doi.org/10.1016/j.ceramint.2012.08.075)
5. Arques Amat A, Garcia-Ripoll AM, et al., (2017) Detoxification and/or increase of the biodegradability of aqueous solutions of dimethoate by means of solar photocatalysis. *J Hazard Mater*. 146: 447-452. [org/10.1016/j.jhazmat.2007.04.046](https://doi.org/10.1016/j.jhazmat.2007.04.046)
6. Arun K J, Batra A K, Krishna A, Bhat K, Aggarwal M D, Joseph Francis P J, (2015) Surfactant Free Hydrothermal Synthesis of Copper Oxide Nanoparticles, *American Jour Mat Sci*, 5(3A), 36-38. doi: 10.5923/s.materials.201502.06
7. Atrak K, Ramazani A, Taghavi Fardood S (2018) A novel sol–gel synthesis and characterization of MgFe₂O₄@ γ -Al₂O₃ magnetic nanoparticles using tragacanth gel and its application as a magnetically separable photocatalyst for degradation of organic dyes under visible light, *J Mater Sci Mater*, 29(8):6702–6710. [org/10.1007/s10854-018-8656-5](https://doi.org/10.1007/s10854-018-8656-5)
8. Bagal MV, Lele BJ, Gogate PR (2013) Removal of 2,4-dinitrophenol using hybrid methods based on ultrasound at an operating capacity of 7L, *Ultrason Sonochem*. 20:1217-1225. [org/10.1016/j.ultsonch.2013.01.015](https://doi.org/10.1016/j.ultsonch.2013.01.015)
9. Balbino TAC, Bellato C R, da Silva AD, de Oliveira Marques Neto J, L de Moura Guimarães (2020) Magnetic cross-linked chitosan modified with ethylenediamine and β -cyclodextrin for removal of phenolic compounds, *Colloids Surf A Physicochem Eng Asp*, 602: 125119-125131. [org/10.1016/j.colsurfa.2020.125119](https://doi.org/10.1016/j.colsurfa.2020.125119)

10. Barka N, Abdennouri M (2011) M.E.L. Makhfouk, Removal of Methylene Blue and Eriochrome Black T from aqueous solutions by biosorption on *Scolymus hispanicus* L.: Kinetics, equilibrium and thermodynamics, Taiwan. Inst. Chem. Eng. 42, 320–326.
11. Caetano M, Valderrama C, Farran A, Cortina J L (2009) Phenol removal from aqueous solution by adsorption and ion exchange mechanisms onto polymeric resins, J Colloid Interface Sci, 338:402-409. [org/10.1016/j.jtice.2010.07.004](https://doi.org/10.1016/j.jtice.2010.07.004)
12. Chong MN, Jin B, Chow CWK (2010) Saint, Recent developments in photocatalytic water treatment technology: a review, Water Res, 44: 2997-3027. [org/10.1016/j.watres.2010.02.039](https://doi.org/10.1016/j.watres.2010.02.039)
13. Chowdhury R, Khan A, Rashid M H (2020) Green synthesis of CuO nanoparticles using Lantana camara flower extract and their potential catalytic activity towards the aza-Michael reaction. RSC Advances, 10(24):14374–14385. [10.1039/D0RA01479F](https://doi.org/10.1039/D0RA01479F)
14. De Luna M D G, Flores ED, Genuino D A D, Futralan C M, Wan M W (2013) Adsorption of Eriochrome Black T (EBT) dye using activated carbon prepared from waste rice hulls—Optimization, isotherm and kinetic studies, J Taiwan Inst Chem Eng, 44(4): 646–653. [org/10.1016/j.jtice.2013.01.010](https://doi.org/10.1016/j.jtice.2013.01.010)
15. Dhanemozhi A C, Rajeswari V, Sathyajothi S (2017) Green synthesis of zinc oxide nanoparticle using green tea leaf extract for supercapacitor application, Mater Today, 4: 660-667. [org/10.1016/j.matpr.2017.01.070](https://doi.org/10.1016/j.matpr.2017.01.070)
16. Etefagh R, Azhir E, Shahtahmasebi N (2013) Synthesis of CuO nanoparticles and fabrication of nanostructural layer biosensors for detecting *Aspergillus niger* fungi, Scientia Iranica 20 (3): 1055-1058. [dorg/10.1016/j.scient.2013.05.015](https://doi.org/10.1016/j.scient.2013.05.015)
17. Fardood ST, Ramazani A, Golfar Z, Joo SW (2017) Green synthesis of Ni-Cu-Zn ferrite nanoparticles using tragacanth gum and their use as an efficient catalyst for the synthesis of polyhydroquinoline derivatives, Appl Organomet Chem, 31:3823-3830. [org/10.1007/s10971-017-4310-6](https://doi.org/10.1007/s10971-017-4310-6)
18. Fardood ST, Ramazani A, Pegah SM, Asiabi A (2017a) Green synthesis of zinc oxide nanoparticles using arabic gum and photocatalytic degradation of direct blue 129 dye under visible light, J Mater Sci Mater Electron. 28 :13596-13601.[doi.1007/s10854-017-7199-5](https://doi.org/10.1007/s10854-017-7199-5)
19. Farhan Hanafi M, Sapawe N (2020) Recyclable study of nickel catalyst with efficient photodegradation of remazol brilliant blue dye. Mater Today, 31: 269-271. [org/10.1016/j.matpr.2020.05.751](https://doi.org/10.1016/j.matpr.2020.05.751)
20. Faungnawakij K, Shimoda N, Fukunaga T, Kikuchi R, Eguchi K (2009) Crystal structure and surface species of CuFe₂O₄ spinel catalysts in steam reforming of dimethyl ether, Appl Catal B, 92, 341-350. [org/10.1016/j.apcatb.2009.08.013](https://doi.org/10.1016/j.apcatb.2009.08.013)
21. Fegade U, Jethave G, Hong W G, et al., (2020) Multifunctional Zn₃Al_{0.4}O_{4.5} crystals: An efficient photocatalyst for formaldehyde degradation and EBT adsorption, Arab J Chem, <https://doi.org/10.1016/j.arabjc.2020.04.002>
22. Franco P, Sacco O, De Marco I, Sannino D, Vaiano V (2020) Photocatalytic Degradation of Eriochrome Black-T Azo Dye Using Eu-Doped ZnO Prepared by Supercritical Antisolvent Precipitation Route: A

- Preliminary Investigation. Top Catal, 63:1193–1205. [org/10.1007/s11244-020-01279-y](https://doi.org/10.1007/s11244-020-01279-y)
23. Geetha MS, Nagabhushana H, Shivananjaiah H N (2016) Green mediated synthesis and characterization of ZnO nanoparticles using Euphorbia Jatropa latex as reducing agent. J Sci Advan Mater and Devi, 1(3): 301–310. [org/10.1016/j.jsamd.2016.06.015](https://doi.org/10.1016/j.jsamd.2016.06.015)
 24. Ghaly AE, Ananthashankar R, Alhattab M, Ramakrishnan VV (2014) Production, characterization and treatment of textile effluents: a critical review, J Chem Eng Process Technol, 5:1-6. DOI: 10.4172/2157-7048.1000182
 25. Gogoi A M, Navgire KC, Sarma P Gogoi (2019) Highly efficient heterogeneous Fenton activities of magnetic β -cyclodextrin (Fe) framework for Eriochrome black T degradation, Mater Chem Phys, 231:233-243. [org/10.1016/j.matchemphys.2019.04.013](https://doi.org/10.1016/j.matchemphys.2019.04.013)
 26. Graham N, Jiang C, Li X, Jiang J, Ma J (2004) The influence of pH on the degradation of phenol and chlorophenols by potassium ferrate, Chemosphere, 56: 949–956. [org/10.1016/j.chemosphere.2004.04.060](https://doi.org/10.1016/j.chemosphere.2004.04.060)
 27. Han C, Yang MQ, Weng B, Xu YJ (2014) Improving the photocatalytic activity and anti-photocorrosion of semiconductor ZnO by coupling with versatile carbon, Phys Chem Phys, 16: 6891-16903, [org/10.1039/C4CP02189D](https://doi.org/10.1039/C4CP02189D)
 28. Heinz D, Hoelderich WF, Krill S, Boeck Huthmacher K (2000) V2O5/TiO2 Catalysts for the Vapor-Phase Oxidation of β -Picoline: Influence of the TiO2-Carrier, J Catal, 192:1–10. [org/10.1006/jcat.1999.2658](https://doi.org/10.1006/jcat.1999.2658)
 29. Honarmand M, Golmohammadi M, Naeimi A (2019) Biosynthesis of tin oxide (SnO2) nanoparticles using jujube fruit for photocatalytic degradation of organic dyes. Adv Powder Technol, 30:1551-1557, [org/10.1016/j.appt.2019.04.033](https://doi.org/10.1016/j.appt.2019.04.033)
 30. Inamuddin Y (2019) Xanthan gum/titanium dioxide nanocomposite for photocatalytic degradation of methyl orange dye, Int J Biol Macromol, 121:1046-1053, [org/10.1016/j.ijbiomac.2018.10.064](https://doi.org/10.1016/j.ijbiomac.2018.10.064)
 31. Jana S, Basu S, Pande S, Ghosh S K, Pal T (2007) Shape-Selective Synthesis, Magnetic Properties, and Catalytic Activity of Single Crystalline β -MnO2 Nanoparticles. J Phys Chem C, 111(44): 16272–16277. [org/10.1021/jp074803l](https://doi.org/10.1021/jp074803l)
 32. Kadam A N, Bhopate DP, Kondalkar VV, Majhi SM, Bathula CD, Tran AV, Lee S.W (2018) Facile synthesis of Ag-ZnO core-shell nanostructures with enhanced photocatalytic activity. J Ind Eng Chem, 61: 78–86. <https://doi.org/10.1016/j.jiec.2017.12.003>
 33. Kansal SK, Sood S, Umar A, Mehta SK (2013) Photocatalytic degradation of Eriochrome Black T dye using well-crystalline anatase TiO₂ nanoparticles, J Alloys Compd, 581: 392–397. [org/10.1016/j.jallcom.2013.07.069](https://doi.org/10.1016/j.jallcom.2013.07.069)
 34. Karade VC, Parit SB, Dawkar VV, Devan RS, Choudhary R J, Kedge V V. ...Chougale AD (2019) A green approach for the synthesis of α -Fe₂O₃ nanoparticles from Gardenia resinifera plant and its In vitro hyperthermia application. Heliyon, 5(7): e02044. [org/10.1016/j.heliyon.2019.e02044](https://doi.org/10.1016/j.heliyon.2019.e02044)
 35. Kaur J, Singhal S (2015) Highly robust light driven ZnO catalyst for the degradation of eriochrome black T at room temperature, Superlattice Microst, 83: 9-21. [org/10.1016/j.spmi.2015.03.022](https://doi.org/10.1016/j.spmi.2015.03.022)

36. Khan A, Liao Z, Liu Y, Jawad A, Ifthikar J, Chen Z (2017) Synergistic degradation of phenols using peroxymonosulfate activated by CuO-Co₃O₄@MnO₂ J Hazard Mater, 329:262–271. doi.org/10.1016/j.jhazmat.2017.01.029
37. Klug P, Alexander LE (1974) X-ray Diffraction Procedures: For Polycrystalline and Amorphous Materials, Wiley, 32: 992-999. org/10.1002/xrs.1300040415
38. Lai MTL, Lai CW, Lee KM, Chook SW, Yang TCK, Chong SH, Juan JC (2019) Facile one-pot solvothermal method to synthesize solar active Bi₂WO₆ for photocatalytic degradation of organic dye. J Alloys Compd, 801:502–510. org/10.1016/j.jallcom.2019.06.116
39. Li K, Ren Y, Lai L, Lai B (2018) Electrolysis assisted persulfate with annular iron sheet as anode for the enhanced degradation of 2, 4-dinitrophenol in aqueous solution, J Hazard Mater, 344:778-787. org/10.1016/j.jhazmat.2017.11.007
40. Li R, Ji Y, Wang J, Li Q, Wu G, Zhang B (2020) Efficient removal of phenol and p-nitrophenol using nitrogen-doped reduced graphene oxide. Colloids Surf A Physicochem Eng Asp, 611:125866-125892. org/10.1016/j.colsurfa.2020.125866
41. Liang S, Teng F, Bulgan G, Zong R, Zhu Y (2008) Effect of phase structure of MnO₂ nanorod catalyst on the activity for CO oxidation, J Phys Chem C, 112:5307-5315. org/10.1021/jp0774995
42. Lin L, Qiu P, Cao X, Jin L (2008) Colloidal silver nanoparticles modified electrode and its application to the electroanalysis of Cytochrome c, Electrochim Acta, 53: 5368–5372. org/10.1016/j.electacta.2008.02.080
43. Liu C, Min Y, Zhang AY, Si Y, Chen JJ, Yu HQ (2019) Electrochemical treatment of phenol-containing wastewater by facet-tailored TiO₂: Efficiency, characteristics and mechanisms, Water Res, 165:114980-114990. org/10.1016/j.watres.2019.114980
44. Liu P, He H, Wei G, Liang X, Qi F, Tan F, Tan W, Zhu J, Zhu R (2016) Effect of Mn substitution on the promoted formaldehyde oxidation over spinel ferrite: catalyst characterization, performance and reaction mechanism, Appl Catal B: Environ, 182: 476-484. org/10.1016/j.apcatb.2015.09.055
45. Ma D, Zhong J, Li J, Wang L, Peng R (2018) Enhanced photocatalytic activity of BiOCl by C70 modification and mechanism insight, Appl Surf Sci, 443, 497-505. org/10.1016/j.apsusc.2018.03.018
46. Mamba G, Mbianda XY, Mishra AK (2015) Enhanced visible light photocatalytic degradation of eriochrome black T and eosin blue shade in water using tridoped titania decorated on SWCNTs and MWCNTs: Effect of the type of carbon nanotube incorporated, Mater Chem Phys, 149–150:734-742. org/10.1016/j.matchemphys.2014.11.035
47. Marjani A, Zare M H, Sadeghi M H, Shirazian S, Ghadiri M (2020) Synthesis of alginate-coated magnetic nanocatalyst containing high-performance integrated enzyme for phenol removal, J Environ Chem Eng, 9:104884-104924. org/10.1016/j.jece.2020.104884
48. Mathew V, Lim J, Kang J, Gim J, Rai AK, Kim J (2011) Self-assembled mesoporous manganese oxide with high surface area by ambient temperature synthesis and its enhanced electrochemical properties, Electrochem Commun, 13: 730-733. org/10.1016/j.elecom.2011.04.023

49. Meng SG, Li D Z, Sun M, Li WJ, Wng J X, Chen J, Fu X Z, Xiao GC (2011) Sonochemical synthesis, characterization and photocatalytic properties of a novel cube-shaped $\text{CaSn}(\text{OH})_6$, *Catal Commun*, 12:972-975. [org/10.1016/j.catcom.2011.02.026](https://doi.org/10.1016/j.catcom.2011.02.026)
50. Mishra S, Soren S, Debnath AK, Aswal DK, Das N, Parhi P (2018) Rapid microwave – Hydrothermal synthesis of CeO_2 nanoparticles for simultaneous adsorption/photodegradation of organic dyes under visible light, *Optik*, 169:125–136. [org/10.1016/j.ijleo.2018.05.045](https://doi.org/10.1016/j.ijleo.2018.05.045)
51. Mu L, Feng SS (2001) Fabrication, characterization and in vitro release of paclitaxel (Taxol) loaded poly (lactic-co-glycolic acid) microspheres prepared by spray drying technique with lipid/cholesterol emulsifiers, *J Control Release*, 76: 239–254. doi: 10.1016/s0168-3659(01)00440-0.
52. Mukherjee S, Roychaudhuri U, Kundu PP (2018) Bio-degradation of polyethylene via complete solubilisation by the action of pseudomonas fluorescens bio-surfactant produced by bacillus licheniformis and anionic surfactant, *J Chem Technol Bio*, 93:1300-1311. [org/10.1002/jctb.5489](https://doi.org/10.1002/jctb.5489)
53. Mustapha S I, Aderibigbe F A, Adewoye T L, Mohammed I A, Odey T O (2020). Silver and titanium oxides for the removal of phenols from pharmaceutical wastewater. *Mater. Today*, 38: 816-822. doi:10.1016/j.matpr.2020.04.669
54. Nayak R, Ali FA, Mishra DK, Ray D, Aswal VK, Sahoo SK, Nanda B (2020) Fabrication of CuO nanoparticle: An efficient catalyst utilized for sensing and degradation of phenol, *J Mater Res Technol*, 9(5):11045–11059. Doi.1016/j.jmrt.2020.07.100
55. Nedkov I, Vandenberghe RE, Marinova T, Thailhades P, Merodiiska T, Avramova I (2006) Magnetic structure and collective Jahn–Teller distortions in nanostructured particles of CuFe_2O_4 , *Appl Surf Sci*, 253:2589-2596. [org/10.1016/j.apsusc.2006.05.049](https://doi.org/10.1016/j.apsusc.2006.05.049)
56. Nezamzadeh-Ejhieh A, Amiri M (2013) CuO supported clinoptilolite towards solar photocatalytic degradation of p-aminophenol, *Powder Technol*, 235:279-288. [org/10.1016/j.powtec.2012.10.017](https://doi.org/10.1016/j.powtec.2012.10.017)
57. Othman I, Haija MA, Ismail I, Zain JH, Banat F (2019) Preparation and catalytic performance of CuFe_2O_4 nanoparticles supported on reduced graphene oxide ($\text{CuFe}_2\text{O}_4/\text{rGO}$) for phenol degradation. *Mater Chem Phys*, 238:121931-121937. [org/10.1016/j.matchemphys.2019.121931](https://doi.org/10.1016/j.matchemphys.2019.121931)
58. Pitarch E, Portoles T, Marin JM, Ibanez M, Albarran F, Hernandez F (2010) Analytical strategy based on the use of liquid chromatography and gas chromatography with triple-quadrupole and time-of-flight MS analyzers for investigating organic contaminants in wastewater, *Anal Bioanal Chem*, 397 (7): 2763-2776. [org/10.1007/s00216-010-3692-x](https://doi.org/10.1007/s00216-010-3692-x)
59. Rachna, Rani M, Shanker U (2018) Enhanced photocatalytic degradation of chrysene by $\text{Fe}_2\text{O}_3@Zn\text{HCF}$ nanocubes, *Chem Eng J*, 348: 754–764. [org/10.1016/j.cej.2018.04.185](https://doi.org/10.1016/j.cej.2018.04.185)
60. Rachna, Rani M, Shanker U (2020) Sunlight assisted degradation of toxic phenols by zinc oxide doped prussian blue nanocomposite, *J Environ Chem Eng*, 8:104040-104052. [org/10.1016/j.jece.2020.104040](https://doi.org/10.1016/j.jece.2020.104040)
61. Rachna, Rani M, Shanker U (2018) Enhanced photocatalytic degradation of chrysene by $\text{Fe}_2\text{O}_3@Zn\text{HCF}$ nanocubes. *Chem Engin J*, 348:754–764. [10.1016/j.cej.2018.04.185](https://doi.org/10.1016/j.cej.2018.04.185)

62. Rachna, Rani M, Shanker U (2019) Sunlight active ZnO@FeHCF nanocomposite for the degradation of bisphenol A and nonylphenol, *J Environ Chem Eng*, 7:103153-1031667. [org/10.1016/j.jece.2019.103153](https://doi.org/10.1016/j.jece.2019.103153)
63. Rachna, Rani M, Shanker U (2020) Synergistic effects of zinc oxide coupled copper hexacyanoferrate nanocomposite: Robust visible-light driven dye degradation, *J Colloid Interface Sci*,584:67-79. [dorg/10.1016/j.jcis.2020.09.079](https://doi.org/10.1016/j.jcis.2020.09.079)
64. Rajakumar G, Thiruvengadam M, Mydhili G, Gomathi T, Chung IM (2018) Green approach for synthesis of zinc oxide nanoparticles from *Andrographis paniculata* leaf extract and evaluation of their antioxidant, anti-diabetic, and anti-inflammatory activities, *Bioprocess Biosyst Eng*, 41:21-30. [10.1007/s00449-017-1840-9](https://doi.org/10.1007/s00449-017-1840-9)
65. Ramazani A, Taghavi Fardood S, Hosseinzadeh Z, Sadri F, Joo SW (2017) Green synthesis of magnetic copper ferrite nanoparticles using tragacanth gum as a biotemplate and their catalytic activity for the oxidation of alcohols, *Iran J Catal*, 7, 181-185.
66. Ramimoghadam D, Hussein MZB, Taufiq-Yap YH (2013) Synthesis and characterization of ZnO nanostructures using palm olein as biotemplate. *Chem Cent J*:7(1) 71-81.doi: 1186/1752-153X-7-71
67. Ramzan M, Obodo R M, Mukhtar S, Ilyas SZ, Aziz F, Thovhogi N (2020) Green synthesis of copper oxide nanoparticles using *Cedrus deodara* aqueous extract for antibacterial activity. *Mater Today*,36, 576-581. doi:10.1016/j.matpr.2020.05.472
68. Rani M, Shanker U (2018) Photocatalytic degradation of toxic phenols from water using bimetallic metal oxide nanostructures, *Colloids Surf A Physicochem Eng Asp*, 553: 546– 561. [org/10.1016/j.colsurfa.2018.05.071](https://doi.org/10.1016/j.colsurfa.2018.05.071)
69. Rani M, Shanker U, (2017) Removal of carcinogenic aromatic amines by metal hexacyanoferrates nanocubes synthesized via green process, *J Environ Chem Eng*, 5:5298– 5311. [org/10.1016/j.jece.2017.10.028](https://doi.org/10.1016/j.jece.2017.10.028)
70. Rani M, Rachna, Shanker U (2018a) Metal hexacyanoferrates nanoparticles mediated degradation of carcinogenic aromatic amines, *Environ Nanotech Monitor Manage*. 10: 36– 50. [org/10.1016/j.enmm.2018.04.005](https://doi.org/10.1016/j.enmm.2018.04.005)
71. Rani M, Rachna, Shanker U (2019) Mineralization of carcinogenic anthracene and phenanthrene by sunlight active bimetallic oxides nanocomposites, *J Colloid Interface Sci*, 555:676– 688.doi.1016/j.jcis.2019.08.016
72. Rani M, Rachna, Yadav J, Shanker U (2020) Efficient degradation of nonylphenol and 2,4-dinitrophenol by sunlight responsive hexacyanocobaltates nanostructures, *Environ Nanotechnol Monit Manag*, 14:100325-100337. [org/10.1016/j.enmm.2020.100325](https://doi.org/10.1016/j.enmm.2020.100325)
73. Rani M, Shanker U (2018b) Removal of chlorpyrifos, thiamethoxam, and tebuconazole from water using green synthesized metal hexacyanoferrate nanoparticles, *Environ Sci Pollut Res*, 11:10878– 10893. <https://doi.org/10.1007/s11356-018-1346-2>
74. Rani M, Shanker U (2018c). Promoting sun light-induced photocatalytic degradation of toxic phenols by efficient and stable double metal cyanide nanocubes. . *Environ Sci Pollut Res*, 25(24): 23764–

23779. <https://doi.org/10.1007/s11356-018-2214-9>

75. Rani M, Shanker U (2020a) Insight in to sunlight-driven rapid photocatalytic degradation of organic dyes by hexacyanoferrate-based nanoparticles. *Environ Sci Pollut Res*, 28: 5637–5650. [.doi:10.1007/s11356-020-10925-7](https://doi.org/10.1007/s11356-020-10925-7)
76. Rani M, Shanker U, Chaurasia A (2017) Catalytic potential of laccase immobilized on transition metal oxides nanomaterials: Degradation of alizarin red S dye, *J Environ Chem Eng*, 5:2730-2739. [org/10.1016/j.jece.2017.05.026](https://doi.org/10.1016/j.jece.2017.05.026)
77. Rani M, Shanker U, Jassal V (2017b) Recent strategies for removal and degradation of persistent & toxic organochlorine pesticides using nanoparticles: A review, *J Environ Manag*, 190: 208–222. [org/10.1016/j.jenvman.2016.12.068](https://doi.org/10.1016/j.jenvman.2016.12.068)
78. Rufus A, Sreeju N, Philip D (2016) Synthesis of biogenic hematite (α -Fe₂O₃) nanoparticles for antibacterial and nanofluid applications, *RSC Adv*, 6: 94206-94217. [org/10.1039/C6RA20240C](https://doi.org/10.1039/C6RA20240C)
79. San N, Hatipoglu A, Koçturk G, Çınar Z (2001) Prediction of primary intermediates and the photodegradation kinetics of 3-aminophenol in aqueous TiO₂ *J Photochem*, 139(2-3): 225–232. [doi.org/10.1016/S1010-6030\(01\)00368-9](https://doi.org/10.1016/S1010-6030(01)00368-9)
80. Satheesh R, Vignesh K, Suganthi A, Rajarajan M (2014) Visible light responsive photocatalytic applications of transition metal (M = Cu, Ni and Co) doped α -Fe₂O₃ nanoparticles, *J Environ Chem Eng*, 2:1956–1968. [org/10.1016/j.jece.2014.08.016](https://doi.org/10.1016/j.jece.2014.08.016)
81. Shahbaz Tehrani F, Daadmehr V, Rezakhani AT, Hosseini R, Akbarnejad Gholipour S (2012) Structural, magnetic, and optical properties of zinc-and copper-substituted nickel ferrite nanocrystals, *J Supercond Novel Magn*, 25: 2443-2455. [doi:1007/s10948-012-1655-5](https://doi.org/10.1007/s10948-012-1655-5)
82. Shamsabadi MK, Behpour M, Babaheidari AK, Saberi Z (2017) Efficiently enhancing photocatalytic activity of NiO-ZnO doped onto nanozeoliteX by synergistic effects of p-n heterojunction, supporting and zeolite nanoparticles in photo-degradation of Eriochrome Black T and Methyl Orange, *J Photochem Photobiol A: Chem*, 346: 133-143. [org/10.1016/j.jphotochem.2017.05.038](https://doi.org/10.1016/j.jphotochem.2017.05.038)
83. Shanker U, Jassal V, Rani M (2016) Catalytic removal of organic colorants from water using some transition metal oxide nanoparticles synthesized under sunlight, *RSC Adv*, 6: 94989-94999. [org/10.1039/C6RA17555D](https://doi.org/10.1039/C6RA17555D)
84. Sharma RK, Ghose R (2016) Synthesis of Co₃O₄–ZnO mixed metal oxide nanoparticles by homogeneous precipitation method, *J Alloy Compound*, 686: 64–73. [org/10.1016/j.jallcom.2016.05.298](https://doi.org/10.1016/j.jallcom.2016.05.298)
85. Sharma S, Bhattacharya A (2016) Drinking water contamination and treatment techniques, *App Water Sci*, 7(3): 1043–1067. [org/10.1007/s13201-016-0455-7](https://doi.org/10.1007/s13201-016-0455-7)
86. Sorbiun M, Mehr ES, Ramazani A, Fardood ST (2018) Green synthesis of zinc oxide and copper oxide nanoparticles using aqueous extract of oak fruit Hull (Jaft) and comparing their photocatalytic degradation of basic violet 3, *Int J Environ Res*, 12: 29-37. [org/10.1007/s41742-018-0064-4](https://doi.org/10.1007/s41742-018-0064-4)

87. Sreekala G, Beevi AF, Resmi V, Beena B (2020) Removal of lead (II) ions from water using copper ferrite nanoparticles synthesized by green method. *Mater Chem Phys*, doi:10.1016/j.matpr.2020.09.087
88. Sukumar S, Rudrasenan A, Padmanabhan Nambiar D (2020) Green-Synthesized Rice-Shaped Copper Oxide Nanoparticles Using *Caesalpinia bonducella* Seed Extract and Their Applications. *ACS Omega*, 5(2):1040-1051. org/10.1021/acsomega.9b02857
89. Tian H, Hu Y, Xu X, Hui M, Hu Y, Qi W, Li ... B (2019) Enhanced wastewater treatment with high o-aminophenol concentration by two-stage MABR and its biodegradation mechanism. *Bioresour Technol*, 289:121649-121657. doi: 1016/j.biortech.2019.121649
90. Tian H, Xu X, Qu J, Li H, Hu Y, Huang L, He W, Li B (2020) Biodegradation of phenolic compounds in high saline wastewater by biofilms adhering on aerated membranes, *J Hazard Mater*, 392: 122463-122474. doi: 1016/j.jhazmat.2020.122463
91. Vazquez-Olmos A, Redon R, Rodriguez-Gattorno G, Mata-Zamora M, Morales-Leal F, Fernandez-Osorio A, Saniger J (2005) One-step synthesis of Mn₃O₄ nanoparticles: structural and magnetic study, *J Colloid Interface Sci*, 291:175-180. org/10.1016/j.jcis.2005.05.005
92. Vijayalakshmi S, Kumar E (2019) Synthesis and Investigations on structural, optical, thermal and electrical conductivity of α -MnO₂ nanoparticles, *JASC*, VI(II), 294-300
93. Villegas LGC, Mashhadi N, Chen M, Mukherjee D, Taylor KE, Biswas NA (2016) Short review of techniques for phenol removal from wastewater, *Curr Poll Reports*, 2:157–167. <https://doi.org/10.1007/s40726-016-0035-3>
94. Wang W, Kan Y, Yu B, Pan Y, Liew K M, Song L, Hu Y (2017) Synthesis of MnO₂ nanoparticles with different morphologies and application for improving the fire safety of epoxy. *Compos Part A Appl Sci Manuf*, 95:173–182.10.1016/j.compositesa.2017.01.009
95. Watanabe H, Koyasu Y (2000) New synthesis route for Mo–V–Nb–Te mixed oxides catalyst for propane ammoxidation, *Appl Catal A*,194–195: 479–485. org/10.1016/S0926-860X(99)00394-4
96. Xue L, Zhang C, He H, Teraoka Y (2007) Catalytic decomposition of N₂O over CeO₂ promoted Co₃O₄ spinel catalyst, *Appl Catal B*, 75:167-174. org/10.1016/j.apcatb.2007.04.013
97. Zafar MN, Amjad M, Tabassum M, Ahmad I, Zubair M (2018) SrFe₂O₄ nanoferrites and SrFe₂O₄/ground eggshell nanocomposites: Fast and efficient adsorbents for dyes removal, *Clean Prod*,199:983–994.doi.1016/j.jclepro.2018.07.204
98. Zeydouni G, Kianizadeh M, Khaniabadi Y O (2018) Eriochrome black-T removal from aqueous environment by surfactant modified clay: equilibrium, kinetic, isotherm, and thermodynamic studies, *Toxin Reviews*, 1556–9551: 1–11.org/10.1080/15569543.2018.1455214
99. Zhao Q, Yan Z, Chen C, Chen J (2017) Spinels: controlled preparation, oxygen reduction/evolution reaction application, and beyond, *Chem Rev*, 117;10121-10211. org/10.1021/acs.chemrev.7b00051
100. Zhong J, Li J, Zeng J, He X, Huang S, Jiang W, Li M (2014) Enhanced photocatalytic activity of In₂O₃-decorated TiO₂, *Appl.Phys A*, 115:1231-1238. org/10.1007/s00339-013-7965-z

Tables

Table 1. Physiochemical properties of selected pollutant

Element	CAS No.	Mol. Mass (g/mol)	Water Solubility (mg/mL)	Appearance	pK _a	Half-life (days)
EBT	1787-61-7	461.381	50	Dark black	6.2, 11.55	-
3-AP	591-27-5	109.13	35	White	4.3, 9.81	15

Table 2. Characteristic properties of green synthesized hetrometallic oxides (HMOs) nanocomposite

S.No	Nanomaterial	Morphology	Surface area (m ² g ⁻¹)	Band gap (eV)	Zeta-potential (mV)
1	CuFe ₂ O ₄	Spherical	35.68	2.1	-23.1
2	CuMn ₂ O ₄	Spherical	30.63	2.4	-22.7
3	MnZn ₂ O ₄	Spherical	10.25	2.6	-22.5

Table 3. Rate constant and half-life values of Eriochrome Black T (EBT) or 3-Aminophenol (3-AP) with the photocatalysts at optimised conditions (*p*-values for fit < 0.05)

Catalyst	CuFe ₂ O ₄			CuMn ₂ O ₄			MnZn ₂ O ₄			Blank*		
	k(h ⁻¹)	t _{1/2} (h)	R ²	k (h ⁻¹)	t _{1/2} (h)	R ²	k (h ⁻¹)	t _{1/2} (h)	R ²	k (h ⁻¹)	t _{1/2} (h)	R ²
EBT	1.1	0.6	0.99	0.8	0.8	0.99	0.6	0.9	0.99	0.03	23	0.89
3-AP	0.7	0.99	0.97	0.5	1.3	0.99	0.4	1.7	0.97	0.02	34	0.94

Note: Triplicate experiments (n=3) were evaluated for estimation of error bar.

*Blank (10 mL of each pollutant with definite concentration without catalyst)

Table 4. Comparison data of Eriochrome Black T (EBT) or 3-Aminophenol (3-AP) degraded reported by other studies

S. No.	Name	Material used	Characterization	Result	Reference
1	EBT (25mgL ⁻¹)	ZnO-CuHCF (15 mg)	PXRD, FT-IR, FESEM-EDS, TEM, BET	Degradation (97–99 %) in sunlight, follow first order kinetics	Rachna et al., 2020
2	EBT	β -cyclodextrin coated Fe ₃ O ₄ (10 ± 2 nm), (60 mg)	PXRD, FTIR, XPS, HR-TEM, SAED, VSM	Degradation (90%) with hydrogen peroxide.	Gogoi et al., 2019
3	EBT (20 mg L ⁻¹)	Tridoped TiO ₂ /CNT (0.1 g)	FE-SEM, EDS, FT-IR, Raman, XRD, UV-Visible	66% removal observed by TOC due to degradation and followed first order kinetics	Mamba et al., 2015
4	EBT (0.08 mM)	ZnO (100 mg)	XRD, HR-TEM, SAED, STEM, EDS, UV-vis, BET	Degradation (92%) in UV light.	Kaur et al., 2015
5	EBT (20 mg L ⁻¹)	NiO-ZnO on nanozeolite X (1g L ⁻¹)	XRD, UV/vis-DRS, FT-IR, TEM and BET	Degradation (85%) in UV sunlight.	Shamsabadi et al., 2017
6	EBT (100 mg L ⁻¹)	Eu-doped TiO ₂ (3 g L ⁻¹)	XRD, SEM, FT-IR, UV-vis,	Degradation (98%) in sunlight	Franco et al., 2020
7	3-AP (10 ⁻⁴ M)	ZnO@FeHCF (20 mg)	PXRD, FT-IR, FESEM-EDS, TEM	Degradation (98%) in sunlight	Rachna et al., 2020
8	EBT (95ppm)	rice hull-based activated carbon (2g)	SEM and IR	93.14% removal by Adsorption	Luna et al., 2013
9	EBT (100mgL ⁻¹)	CuO (0.02g)	XRD, SANS, FTIR, UV-vis, SEM	98% degradation in 60 min followed first order kinetics	Nayak et al., 2020
10	AP (100 g/L)	iron nano-adsorbent (5mg/10mL)	FT-IR, XRD, SEM and TEM	80% removal by Adsorption	Alharbi et al., 2018
11	3-AP (10 ⁻⁴ M)	NiCuO, CuCr ₂ O ₄ and NiCrO ₃	PXRD, FT-IR, FE-SEM, EDS, TEM, BET, PL	Degradation (97%) in sunlight	Rani and Shanker, 2018

		(15 mg)			
12	3-AP (20 mgL ⁻¹)	CuO supported Clinoptilolite (2.0 gL ⁻¹)	XRD, FT-IR, BET, SEM	Degradation (60%) in sunlight	Nezamzadeh Ejhieh et al., 2013
13	AP (200 mg/L)	N-doped r- G.O (80.60 mg/g)	FE-SEM, HR-TEM, TGA, FT-IR, XPS,	Removal greater than 80% via adsorption and follow Pseudo first order kinetics	Zhao et al., 2020
14	AP (1.5 Mm)	magnetic alginate-coated nanoparticles	SEM, TEM, FT-IR, XRD	98.1% via separation technique	Marjani et al., 2020
15	AP	Fe/CLCh-EDA/β-CD	IR, XRD, Raman, AAS,	90.1 % removal via adsorption and follow pseudo first, pseudo second order kinetics	Balbino et al., 2020
16	AP	Ag/Ti co-doped activated carbon (0.1 g/50 mL)	HRSEM, EDS, XRD, and FTI	99.86% removal via adsorption and followed pseudo-second order model	Mustapha et al., 2020
18	EBT,3A-P (20mgL ⁻¹)	CuFe ₂ O ₄ , CuMn ₂ O ₄ , MnZn ₂ O ₄ (80 mg)	PXRD, FT-IR, FE-SEM, HR-TEM, XPS, BET	97% dye degradation, 93% phenol degradation	Present Study

Figures

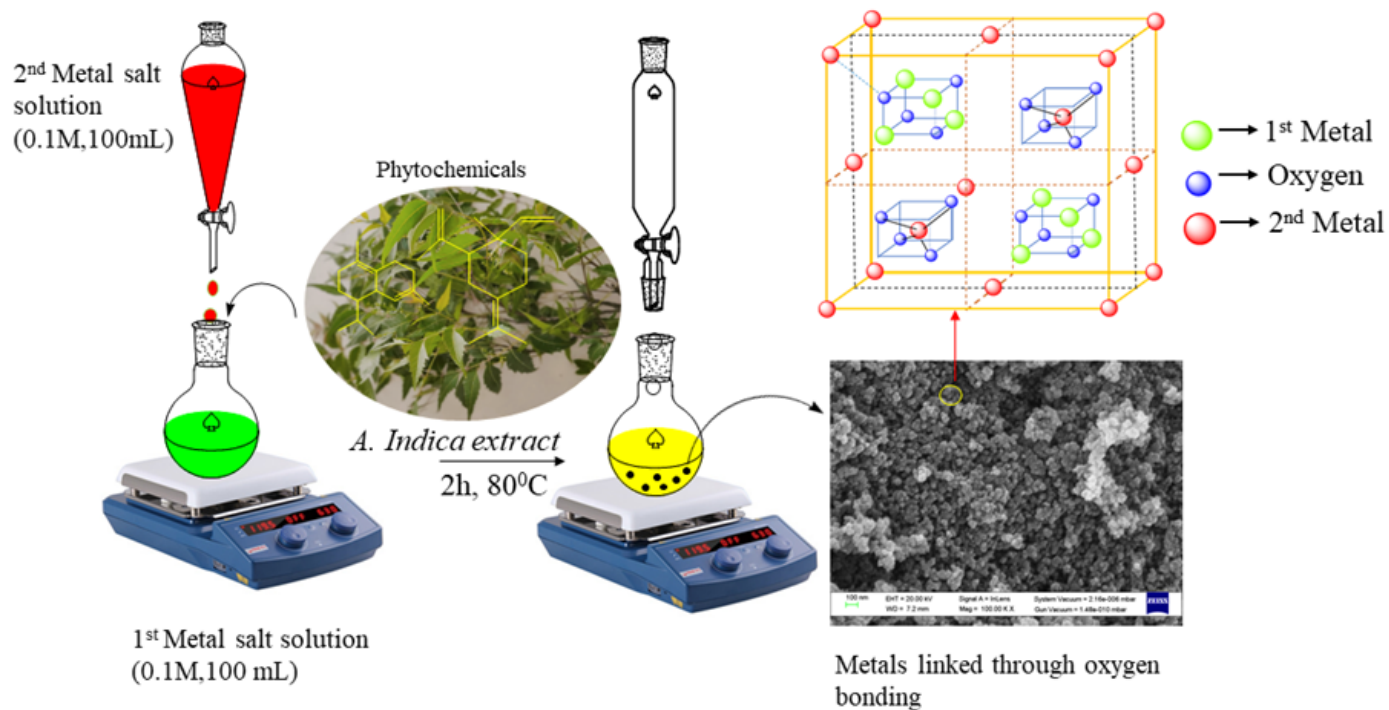


Figure 1

Possible representation of synthesis of the photoactive nanocomposite by using *Azadirachta indica* plant extract

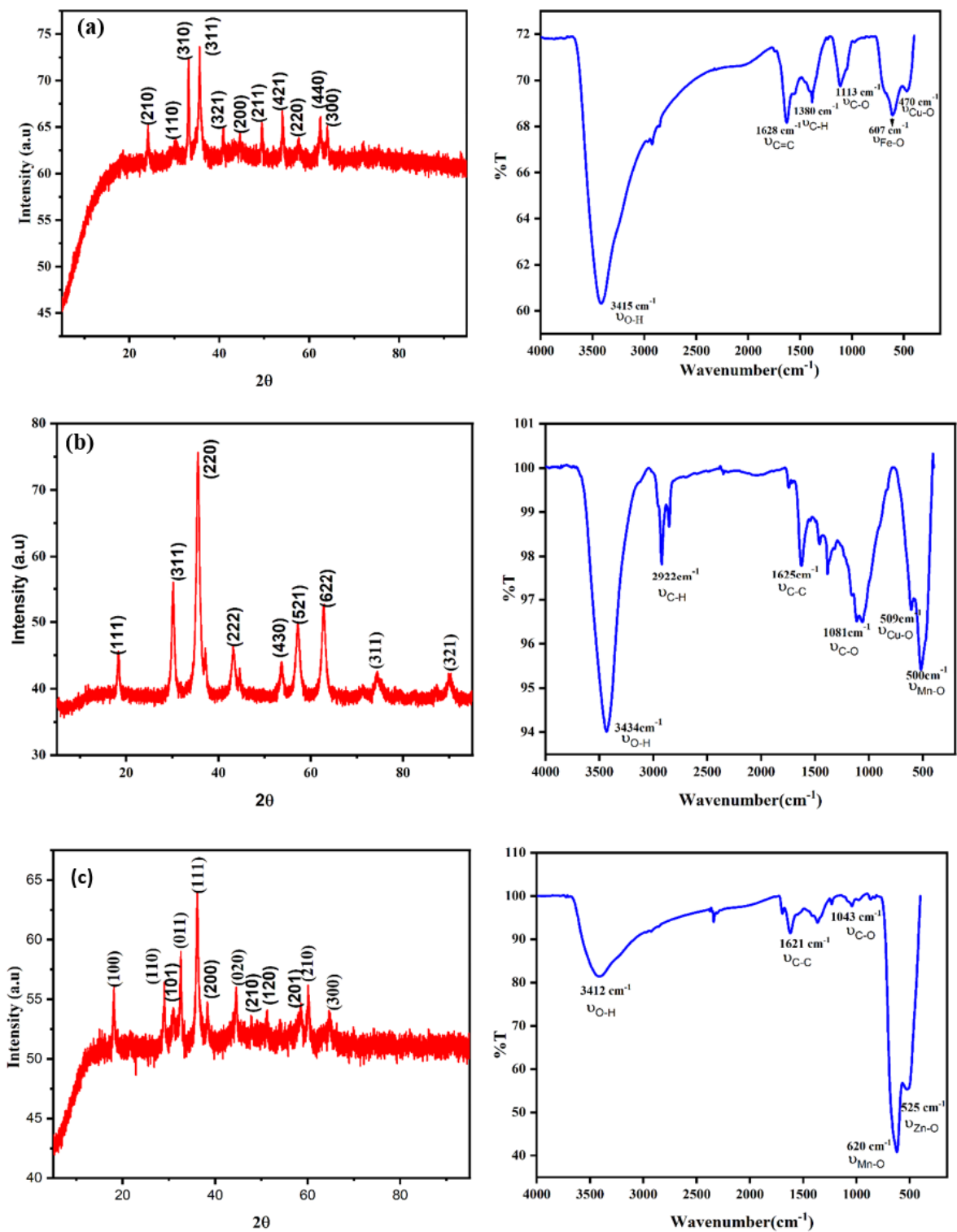


Figure 2

Powdered X-ray Diffraction (PXRD) and FT-IR spectra (a) CuFe₂O₄ (b) CuMn₂O₄ (c) MnZn₂O₄.

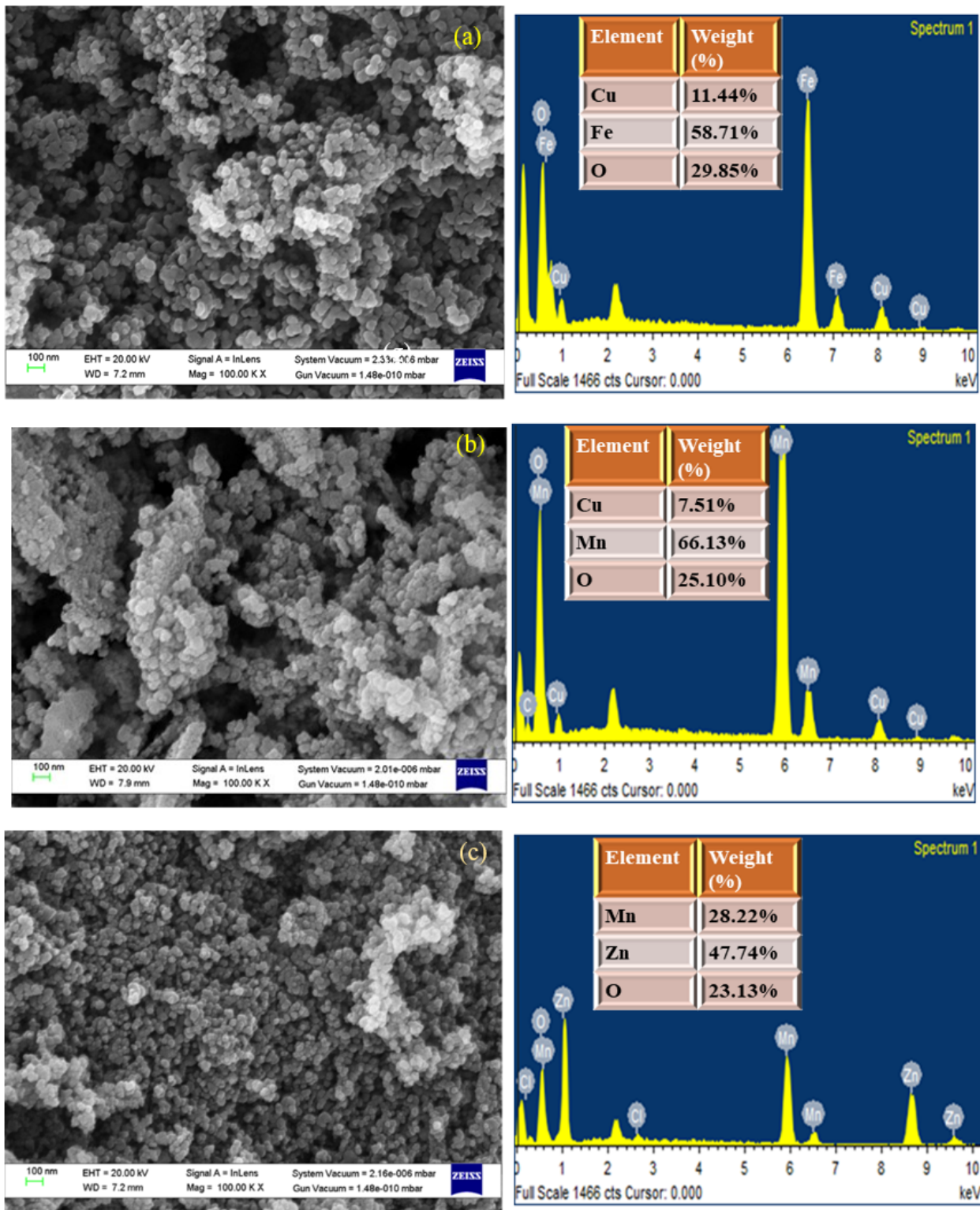


Figure 3

FE-SEM images of with (EDS) and Size histogram (a) CuFe₂O₄ (b) CuMn₂O₄ (c) MnZn₂O₄

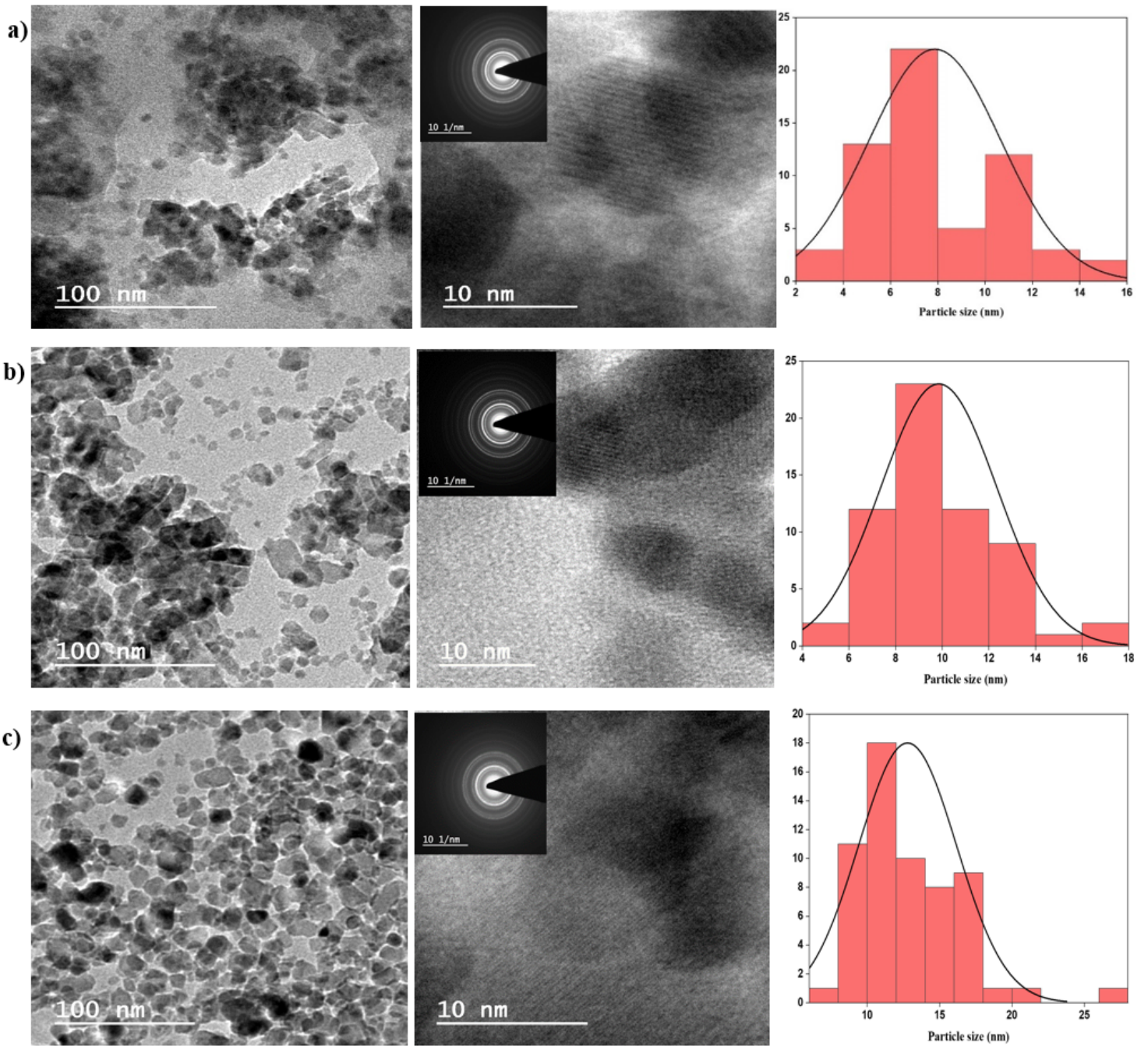


Figure 4

Represents TEM images of (a) CuFe_2O_4 (b) CuMn_2O_4 (c) MnZn_2O_4 with SAED figure

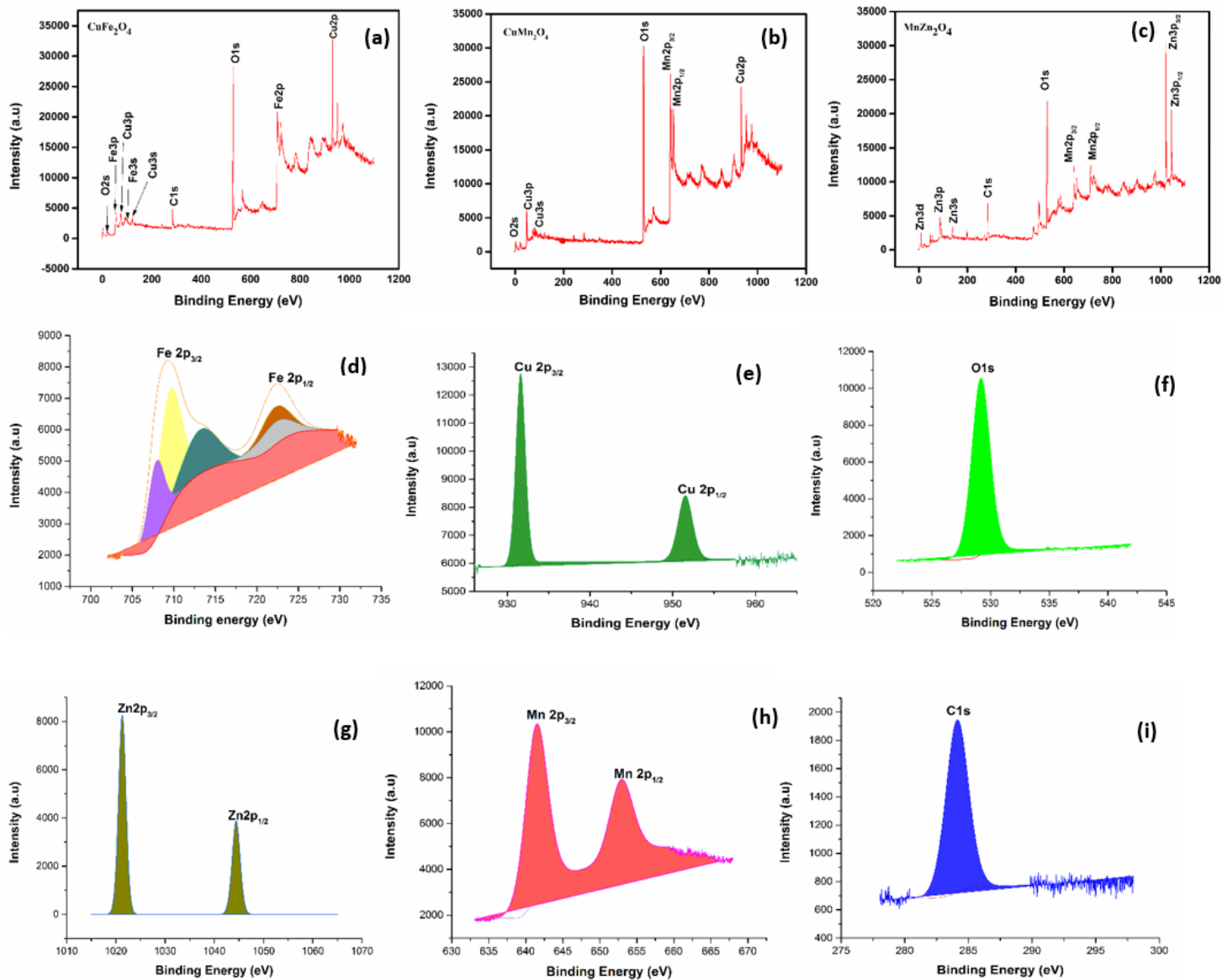


Figure 5

XPS analysis of (a) CuFe_2O_4 , (b) CuMn_2O_4 , (c) MnZn_2O_4 and deconvoluted short scan spectra of (d) Fe2p, (e) Cu2p, (f) O1s, (g) Zn2p, (h) Mn 2p, (i) C1s.

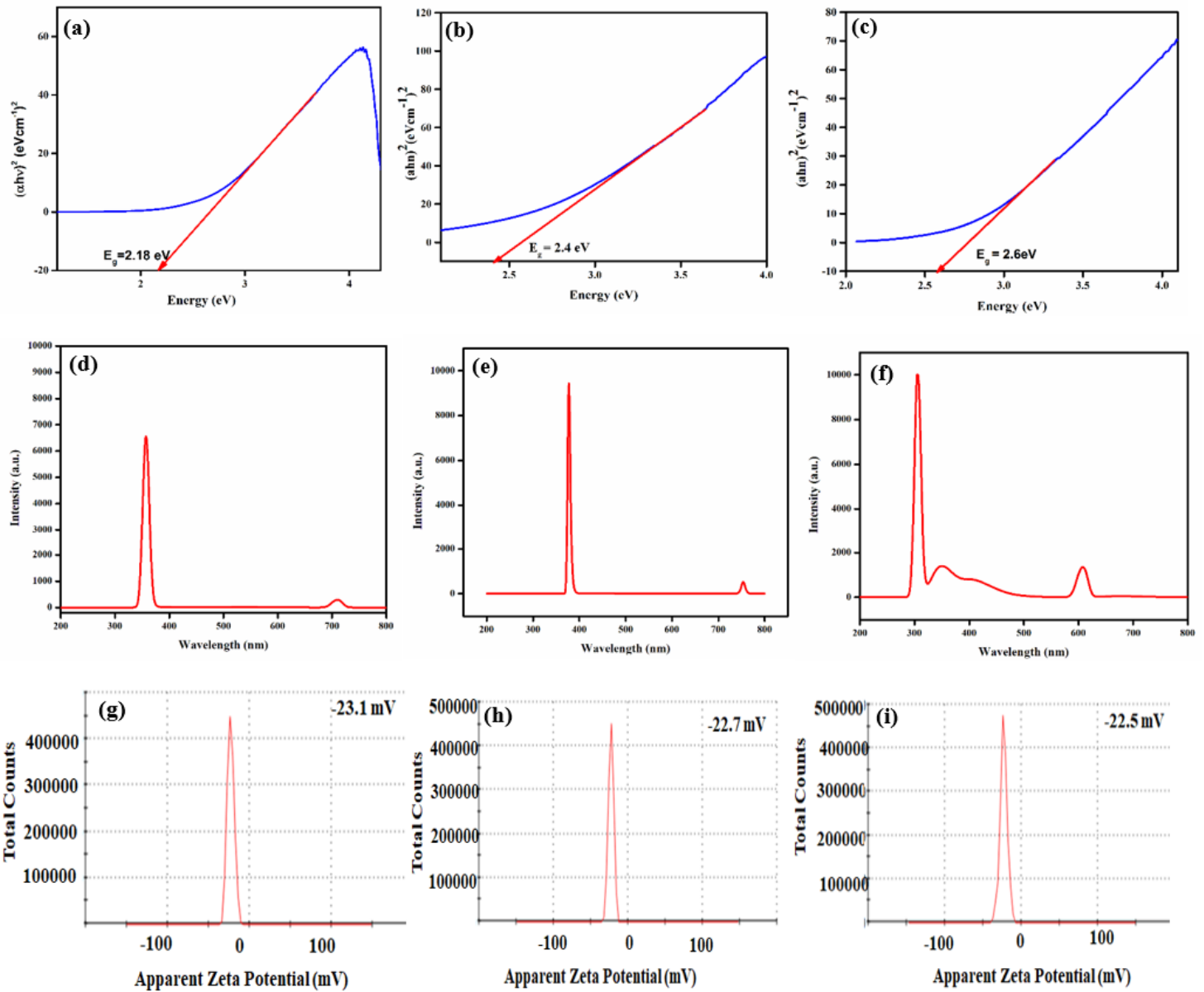


Figure 6

Represents the measured band gap by using Tauc equation of (a) CuFe₂O₄ (b) CuMn₂O₄ (c) MnZn₂O₄ Photoluminescence (PL) spectra of (d) CuFe₂O₄ (e) CuMn₂O₄ (f) MnZn₂O₄. Zeta-potential spectra of (g) CuFe₂O₄ (h) CuMn₂O₄ (i) MnZn₂O₄

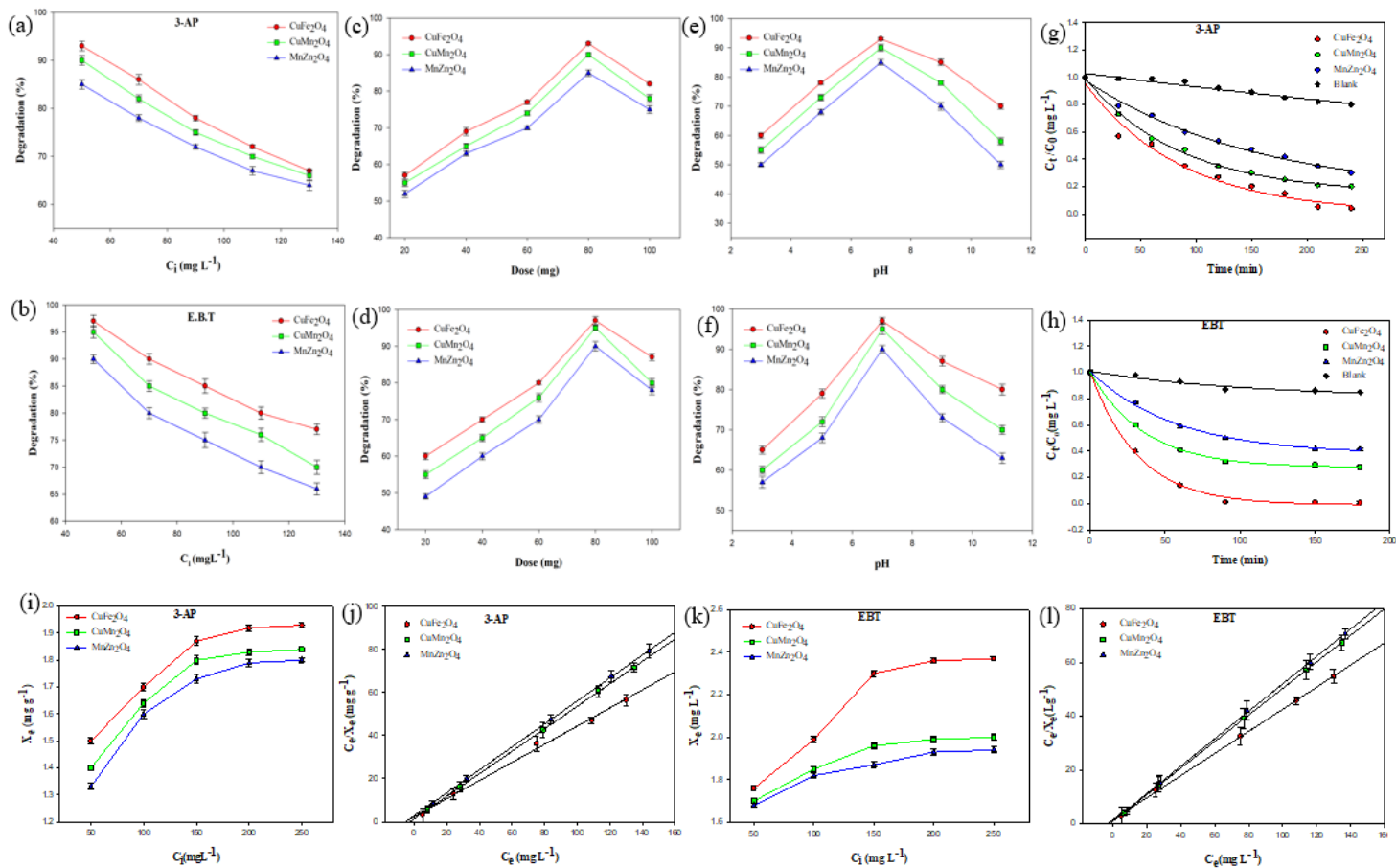


Figure 7

Percentage degradation of 3-aminophenol (3-AP) and Eriochrome Black T (EBT) on HMOs at (a),(b) concentrations dependent (c),(d) catalyst dosages. (e), (f) pH. Reaction kinetics of 3-AP(g) and (h) EBT dye. Langmuir adsorption isotherm model (i),(j) 3-AP (k),(l) EBT dye Note: Triplicate experiments ($n = 3$) were evaluated for estimation of error bar

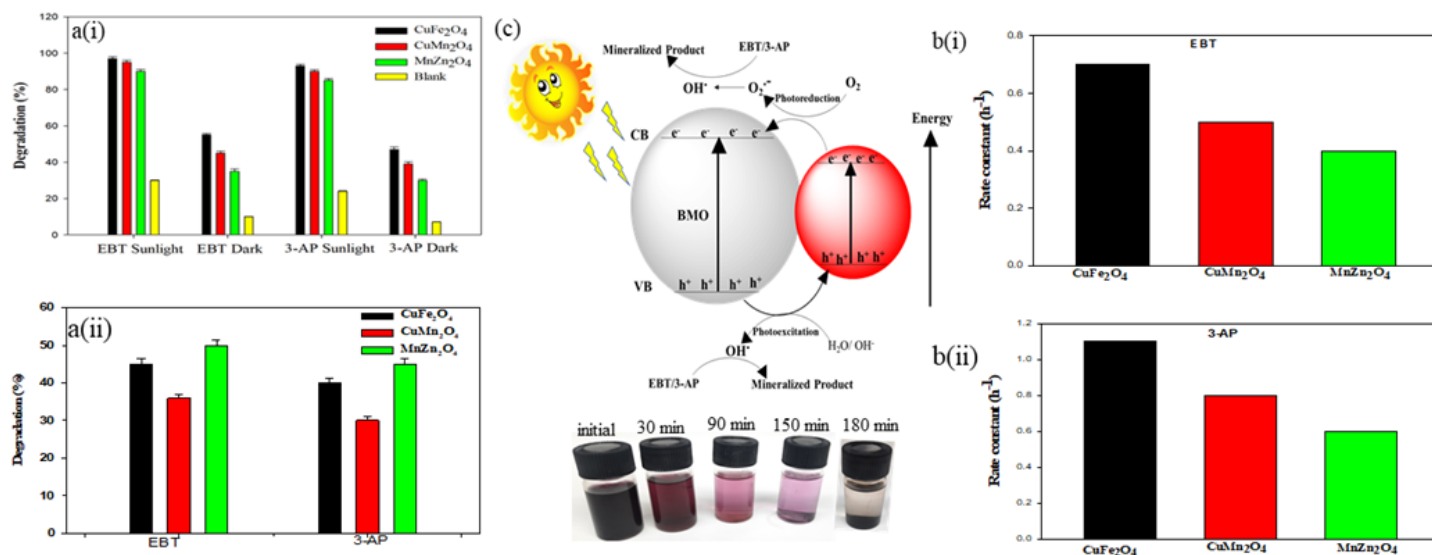


Figure 8

a (i) Source dependent study of 3-Aminophenol (3-AP) and Eriochrome Black T (EBT). a (ii) Effect of radical quenchers on the degradation ability of heterometallic oxides (HMOs) nanocatalysts. b (i) and b (ii) rate constant bar graph of EBT dye and 3-AP (c) Schematic representation of charge separation mechanism for degradation (d) (e). Note: Triplicate experiments ($n = 3$) were evaluated for estimation of error bar.

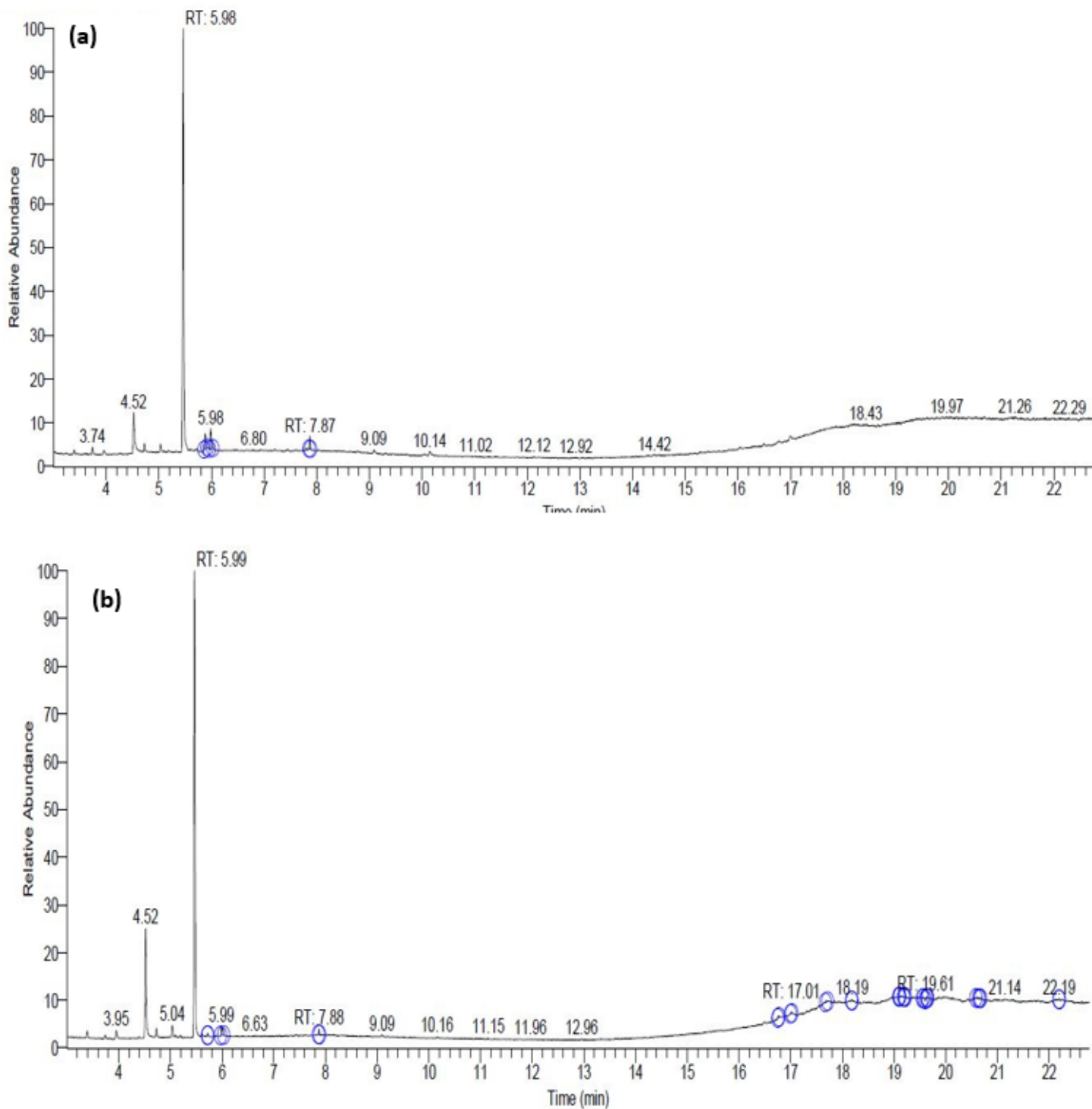


Figure 9

Total Ion Chromatograph (a) Eriochrome Black T (EBT) and (b) 3-aminophenol (3-AP)

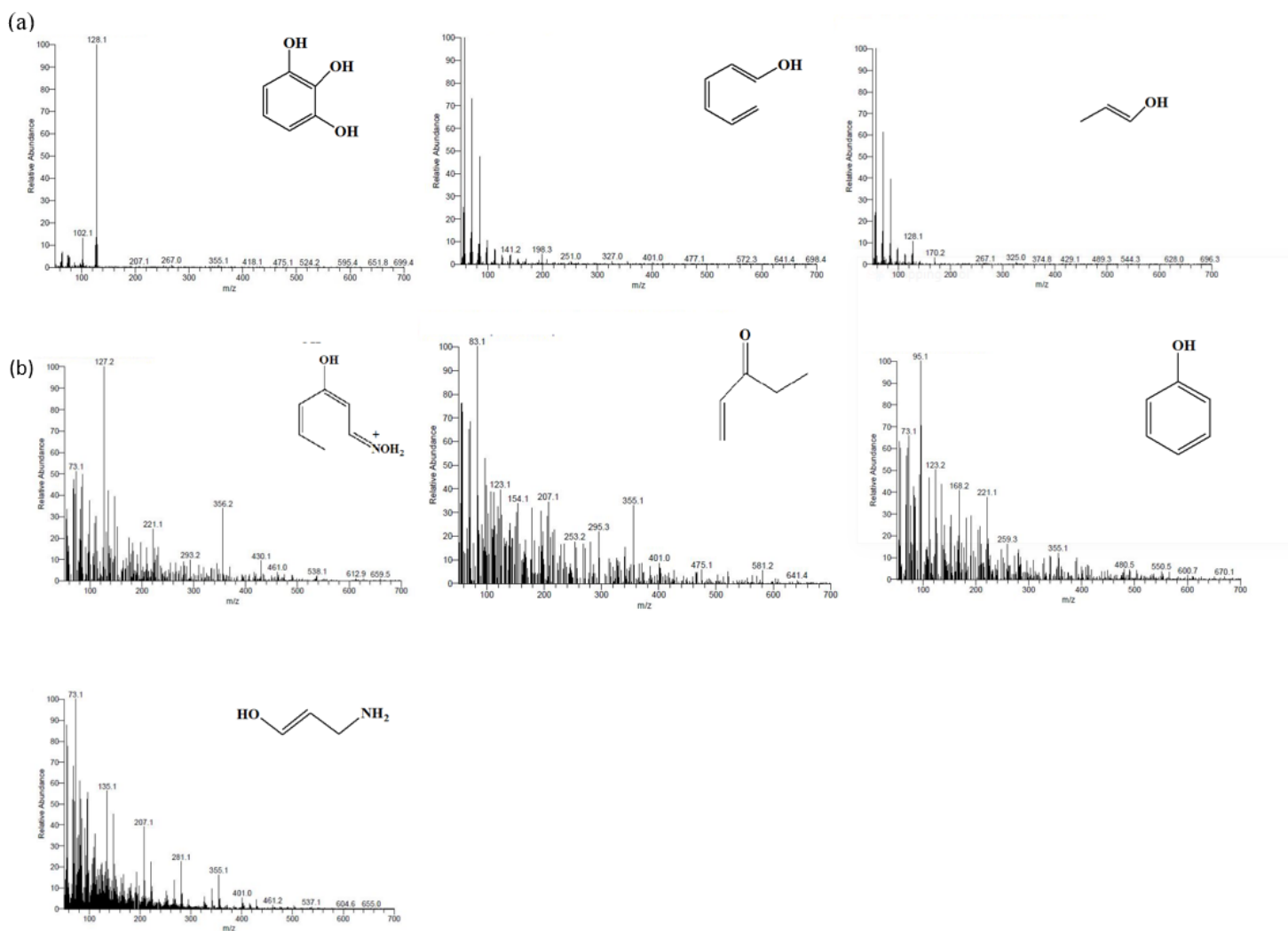


Figure 10

Representative mass spectrum of the degraded products formed of (a) EBT dye and (b) 3-AP over HMOs nanocomposite.

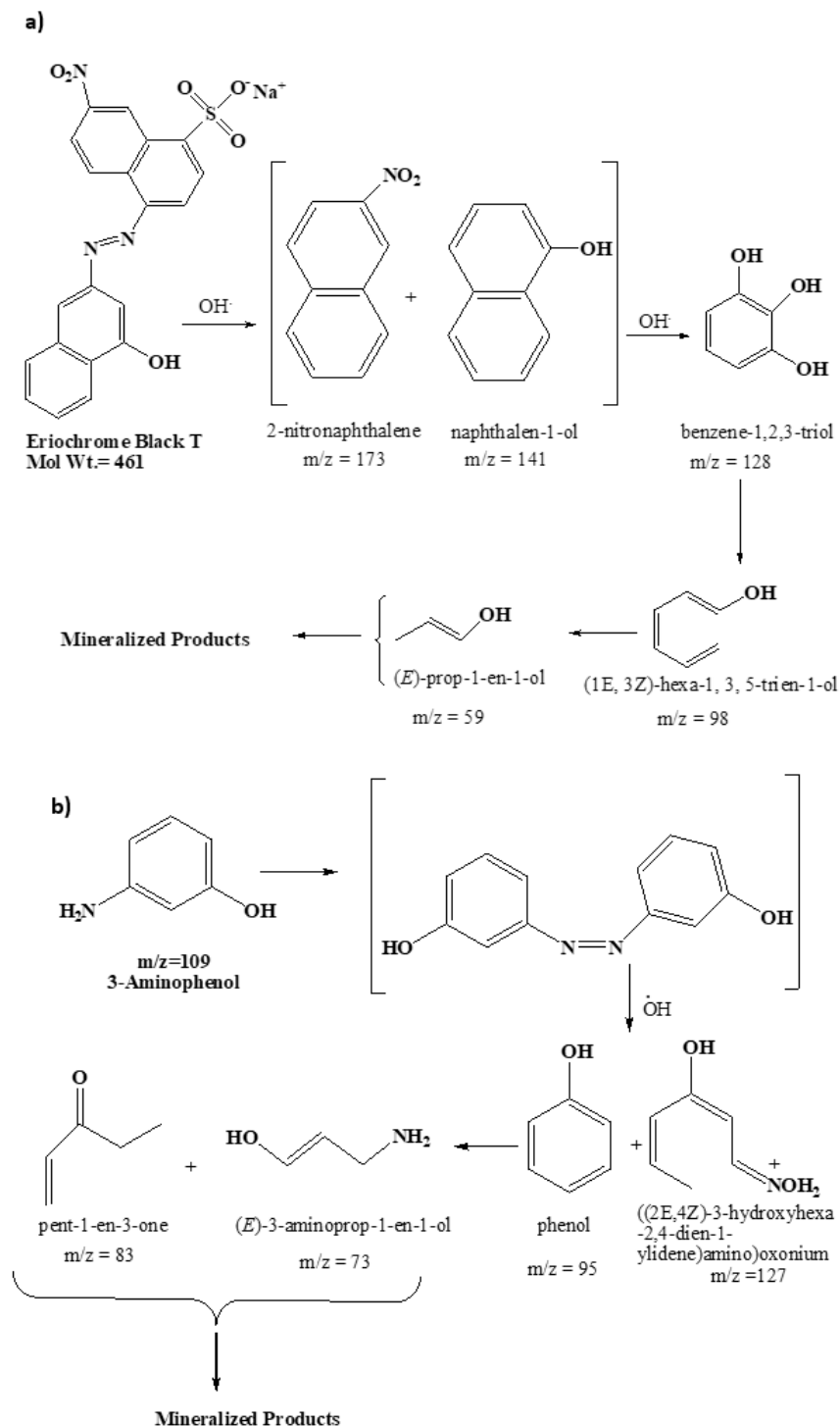


Figure 11

Proposed degradation pathway for the degradation of (a) Eriochrome Black T (EBT) and (b) 3-Aminophenol (3-AP) over Heterometallic oxides (HMOs) nanocomposite (Concentration; 50 mg L⁻¹; pH: ~7; catalyst dose: 80 mg; natural sunlight; time 3h)

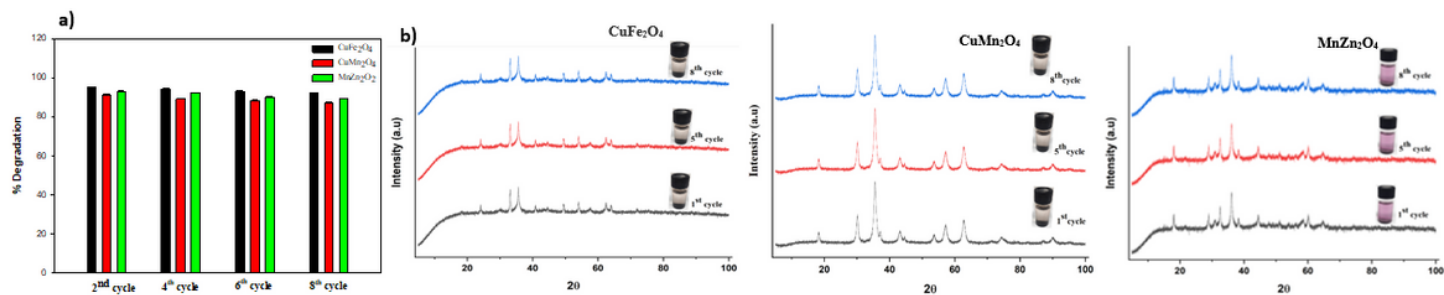


Figure 12

(a) Reusability analysis of Heterometallic oxides (HMOs) nanoparticles for Eriochrome Black T (EBT) and 3-Aminophenol (3-AP) degradation; (b) XRD pattern of CuFe₂O₄, CuMn₂O₄ and MnZn₂O₄ photocatalysts up to 10 cycle. 1st

Supplementary Files

This is a list of supplementary files associated with this preprint. Click to download.

- [SupportingInformation.docx](#)